SYNTHESIS AND THE STRUCTURAL, CHEMICAL, AND ELECTRICAL CHARACTERIZATION OF $AL_{1-X}SC_XN$ SOLID-SOLUTIONS FOR PIEZOELECTRIC AND FERROELECTRIC THIN FILM APPLICATIONS

A Dissertation
Presented to
The Academic Faculty

by

[John Allen Wellington-Johnson]

In Partial Fulfillment
of the Requirements for the Degree
[MASTER OF SCIENCE] in the
[SCHOOL OF MATERIALS SCIENE & ENINGEERING/
COLLEGE OF ENGINEERING]

Georgia Institute of Technology
[05/2025]

SYNTHESIS AND THE STRUCTURAL, CHEMICAL, AND ELECTRICAL CHARACTERIZATION OF $AL_{1-X}SC_XN$ SOLID-SOLUTIONS FOR PIEZOELECTRIC AND FERROELECTRIC THIN FILM APPLICATIONS

Approved by:

Dr. Lauren M. Garten, Advisor
School of Materials Science & Engineering
Georgia Institute of Technology

Dr. Eric Vogel
School of Materials Science & Engineering
Georgia Institute of Technology

Dr. Mark Losego
School of Materials Science & Engineering
Georgia Institute of Technology

Date Approved: [05 30, 2025]

[To Sharon and Nadine, of course]

ACKNOWLEDGEMENTS

My first acknowledgments must, of course, be to my mother, my grandmother, my older brother, my father, my friends, and to the support of so many others. This work represents just some of the skills and experiences I have been able to take away from my years at Georgia Tech, this has been a very enjoyable time of my life. I am sure I have made life-long friends and memories during my journey here. None of this would not have been possible without the support and encouragement of the many smiling faces that make up my life. I have found so many people who want to see my success ; I have found so much love on this journey.

I would like to express my gratitude to my advisor, Dr. Lauren Garten, who introduced me to the field of ferroelectrics, and gave me a playground of tools to conduct my research. None of this work would have been possible without her support. I have learned many things from Lauren, and I am always in awe at the depth of her knowledge and how quickly she can process and articulate thoughts on difficult subject matter. I will always admire her sternness and her passion for excellence. My sincere thanks go out to Dr. Losego and Dr. Vogel as well for their expertise, support, and encouragement in this defense process.

I would like to extend my gratitude to Dr. Dingreville and Dr. Vizoso from the Center for Integrated Nanotechnologies of Sandia National Laboratories – their help in winning a user-grant and in developing phase-field simulations were intellectually stimulating and helped me learn more on the physics and theory of ferroelectrics. I would also like to extend gratitude to Dr. Freeman, Dr. Stheins, and Dr. Dekkers of LAM

Research Corporation - for their interest in me and in supporting me as the company sponsor for the GEM fellowship – their encouragement, mentorship, and industry knowledge were invaluable.

To my Tribology team at Sandia (Tribo-Force One!), I will be forever thankful for the encouragement and help in preparing my National Science Foundation (NSF) Graduate Research Fellowship Award application, I treasure and reflect fondly on my time in Albuquerque. To Tito, Dr. Shin, Dr. Collins, and of course the Black Leadership Committee of Sandia National Labs – thank you for the encouragement to go after my M.Sc. in Mechanical Engineering at the University of New Mexico, and for being just as encouraging when I wanted to pursue new horizons at Georgia Tech.

I thank all of these outstanding professors for their inspiration, support, and guidance on my journey here and on my thesis. An additional thanks to the National Science Foundation and the GEM Consortium whose graduate fellowship awards made this all possible.

I would like to thank the staff at the Microelectronic Research Center and the Materials Characterization Facility at Georgia Tech for the SEED grant and for their outstanding roster of staff. Todd Walters, David Tavakoli, Walter Henderson, Rathi Monikandan, Weston Straka, Gray Spinner, Vinh Nguyen, Dr. Durga R. GaJula, Dr. Hang Chen, Dr. Chris Yang, Charlie Suh, and Charlie Turgeon - I cannot thank them enough for all their help in the cleanroom, their training, and their dedication to ensuring the tools operation.

The timeless discussions and knowledge exchanged with my friends and fellow lab-mates have been invaluable to my research during the past few years. A special thanks to Marshall Frye, Ian Graham, and Jonathan Chin for their comradery, and for being instrumental to my growth and development here. I wish to thank the other members of our lab too: Fariha Rubiya, Kayla Chuong, Yang Liu, Bonnie Gardner, Roxeanne Ware, Joshua Wahl, Anaranya Ghorai, and Dr. Olsterholm, with special thanks to my undergraduate Tianqi Sun and a nod to my NSF-Research Experience for Teachers mentee Surekha Prasad, along with my Summer Undergraduate Research Experience mentees Danny and Jacob. I have such fond memories with every name mentioned. I could not have done this journey without the support and cooperation of everyone mentioned.

Last but not least, a hearty thank you to my parents, Sharon Wilkins and Carvin Johnson, who have given me their unyielding love and support. My older brother AJ is my rock and I'm so proud of him ; my late grandmother Madine, my Salisbury family, and my Crump lineage will always have my heart. These are the people who have shaped me into the person that I am now and have never stopped encouraging me through the entirety of this journey. With endless love and thanks to my family and the acknowledged.

TABLE OF CONTENTS

LIST OF TABLES

LIST OF FIGURES

SUMMARY

Piezoelectric and ferroelectric thin-film materials are integral to a wide range of modern electronic systems, enabling the functionality of RF filters, LIDAR systems, gyroscopes, micromachined ultrasonic transducers, computer memory, and device switches. As devices shrink and performance demands rise, there is growing interest in enhancing the piezoelectric and ferroelectric properties of material's while maintaining compatibility with silicon and CMOS processes. Aluminum nitride (AlN), a CMOS-compatible, wide bandgap material, is widely used in resonators and filters due to its strong piezoelectric response, thermal stability, and low dielectric and acoustic losses, which together enable high electromechanical coupling and quality factor. Substituting scandium (Sc) into the AlN lattice to form $Al_{1-x}Sc_xN$ increases lattice distortion and internal strain sensitivity, enhancing the longitudinal piezoelectric coefficient (d_{33}) and effective electromechanical coupling (k_t,eff^2) by up to 400%. However, Sc substitution also introduces a structural trade-off, as increasing content beyond a critical threshold ($x \approx 0.43$) induces a phase transition from the polar wurtzite phase to a non-polar cubic structure, diminishing piezoelectric performance.

The two major aims of this thesis defense are to understand how Sc target power influences the composition and crystallinity of co-sputtered AlScN films and to examine how sputtering mode affects the ferroelectric behavior of $Al_{75}Sc_{25}N$. Increasing Sc target power from 100 W to 150 W raises the Sc content from 17 at% to 27 at% and results in greater oxygen uptake and reduced c-axis crystallinity. Separately, by holding all deposition parameters constant and varying the sputtering mode (DC, RF, and mixed

RF+DC), this work demonstrates that deposition energetics strongly influence ferroelectric response - RF sputtering yields strong polarization switching, while DC sputtering results in films with primarily dielectric behavior. These findings provide a foundation for optimizing AlScN thin films for next-generation piezoelectric and ferroelectric MEMS devices.

CHAPTER 1. INTRODUCTION

Piezoelectric thin-film materials are foundational to modern electronic systems[1,2]. Piezoelectric materials enable key functionalities in devices such as RF filters[3], gyroscopes[1], LIDAR systems[4,5], microphones, and micromachined ultrasonic transducers (pMUTs)[4–6]. Increasingly, electronic devices are getting smaller and gaining more complexity while simultaneously requiring more external power. With the increasing performance demands and concurrent miniaturization, there is a growing need for enhanced piezoelectric properties in modern thin film materials while still having compatibility to silicon (Si) and complementary-metal-oxide-semiconductor (CMOS) processing.

Aluminum Nitride (AlN) is a wide band gap (E_g> 6.2 eV)[1] piezoelectric material with a stable piezoelectric response above 1000°C [4]. AlN is dominant in piezoelectric resonators and filters in part due to its CMOS compatibility[5] along with its low dielectric and acoustic losses,[3] which enables high-quality factor in devices.[3] AlN has a hexagonal wurtzite ($a = b \neq c$) crystal structure ($P6_3mc$ space group) with the a-lattice constant ranging from (3.110 Å to 3.113 Å) and the c-lattice constant ranges from (4.978 Å to 4.982 Å)[5,7]. AlN exists in three different phases, namely rocksalt, zincblende, and wurtzite phase, with the wurtzite phase being the most stable.[8]

The substitution of scandium (Sc) for aluminum (Al) to form aluminum scandium nitride ($Al_{1-x}Sc_xN$ or AlScN) has been shown to enhance the piezoelectric response.[4,8] Aluminum and scandium have the same valence state which allows for the Sc ion to substitute into the system while maintaining charge neutrality. The Sc atom (radius = 160 pm) is slightly larger than Al atom (radius = 118 pm) and more electronegative, Sc atoms tend towards a layered hexagonal structure as well, and thus substituting Al with Sc increases lattice parameters of the unit cell especially in c-axis[9]. Substituting Sc in for Al has also been shown to soften the metal-nitrogen bond.[10] The structural changes and increase in the c-axis lattice parameter from the scandium incorporation, increase the longitudinal piezoelectric coefficient (d_{33}) (i.e., the charge generated per unit stress along the same axis as the applied force) by up to 400% [11,12] and improves the electromechanical coupling coefficient (k_t,eff²) [13] (i.e., quantifies the efficiency of energy conversion between electrical and mechanical domains in piezoelectric materials) for microelectromechanical-systems (MEMS) and RF applications. The non-centrosymmetric $P6_3mc$ wurtzite phase extends to compositions with scandium incorporation less than x=0.5 ($A_{1-x}Sc_xN$) beyond which the rocksalt-type phases becomes more stable . [8] The non-piezoelectric centrosymmetric cubic rock-salt phase occurs at percentages over $x > 0.5$. [8] The piezoelectric properties of AlScN increase with Sc content up to an experimentally determined critical threshold of ($x \approx 0.43$).[8,14]

This work investigates the synthesis and characterization of AlScN solid solutions deposited via both reactive DC-pulsed magnetron co-sputtering (using ceramic AlN and metallic Sc targets) and from a stoichiometric $Al_{75}Sc_{25}N$ target. Films were deposited on a variety of structural and conductive substrates, including (100) Si, and bottom electrodes such as (0002) Hf, with out-of-plane lattice mismatches ranging from 2–40% - this approach enabled the exploration of film synthesis growth with and without seed layers. Sc content was varied up to x = 0.27 in co-sputtered films from the AlN and Sc targets, where the Sc target power is used to vary resultant film Sc concentration. Key film characteristics including crystal orientation, grain morphology, surface roughness, surface and bulk composition, and the chemical response of the films ferroelectric behavior were assessed.

Chapter 2 of this Masters thesis explores the material characterization of $Al_{1-x}Sc_xN$ solid solutions synthesized through the mixed mode (RF+DC) co-sputtering of AlN and Sc targets. This work describes the impact of increasing Sc target power on the resulting composition and microstructure of AlScN thin films deposited without a seed layer. As the Sc target power is increased from 100 W to 150 W, XPS results show that the Sc concentration increases from 17 at % to 27 at % Sc with an increase in oxygen from 15 at % to 21 at % oxygen content, with chemical analyses revealing nitride and oxynitride bonding. Films grown at 100 and 125 W Sc target power exhibit solely the wurtzite hexagonal phase of AlScN with (0002) out-of-plane orientation. Increasing the Sc content further reduces the c-axis crystallinity of the AlScN thin films as indicated by the full-width-half-max (FWHM) of the rocking curves increasing.

Chapter 3 of this Masters thesis investigates the ferroelectric and dielectric properties of $Al_{75}Sc_{25}N$ thin films deposited using different sputtering modes: DC, RF, and RF&DC co-sputtering. This work isolates the effect of deposition energetics by holding all other conditions constant while varying the sputter method. Clear ferroelectric switching behavior is observed in films deposited via RF sputtering, with an average remnant polarization (P_R) of 98 µC/cm² and a coercive field (E_C) of 4.6 MV/cm. In contrast, DC sputtered films exhibit primarily linear dielectric characteristics, suggesting the absence of ferroelectric switching. Co-sputtered films deposited with mixed RF&DC power show an intermediate response, with reduced PR and EC compared to RF films, but with a larger separation between EC and breakdown field (E_{BD}), highlighting the trade-offs between ferroelectric strength and device robustness. This chapter demonstrates that the sputtering mode plays a critical role in tuning the functional response of AlScN films and presents mixed-mode sputtering as a promising route for enhancing ferroelectric reliability in thin-film devices. The findings contribute to a deeper understanding of the structure–property relationships in AlScN films and offer pathways to optimize their piezoelectric and ferroelectric properties.

This work describes the impact of increasing scandium target power on the resulting composition and microstructure of $Al_{1-x}Sc_xN$ thin films deposited without a seed layer. As the Sc target power is increased from 100 W to 150 W, XPS results show that the Sc concentration increases from 17 at % to 27 at % Sc with an increase in oxygen from 15 at % to 21 at % oxygen content. Films grown at 100 and 125 W Sc target power exhibit solely the wurtzite phase of AlScN with (0002) out-of-plane orientation. Increasing the Sc content further reduces the c-axis crystallinity of the AlScN thin films as indicated by the full-width-half-max (FWHM) of the rocking curves increasing. This work provides an analysis of the evolving chemical response of the film elements as Sc target power is changed and underscores the critical role of Sc target power in tuning both composition and structural quality in AlScN thin films.

CHAPTER 2. IMPACT OF SCANDIUM TARGET POWER ON THE MICROSTRUCTURE AND CHEMICAL RESPONSE OF CO-SPUTTERED $AL_{1-X}SC_XN$ THIN FILMS

2.1 Abstract

This work describes the impact of increasing scandium target power on the resulting composition and microstructure of $Al_{1-x}Sc_xN$ thin films deposited without a seed layer. As the Sc target power is increased from 100 W to 150 W, XPS results show that the Sc concentration increases from 17 at % to 27 at % Sc with an increase in oxygen from 15 at % to 21 at % oxygen content. Films grown at 100 and 125 W Sc target power exhibit solely the wurtzite phase of AlScN with (0002) out-of-plane orientation. Increasing the Sc content further reduces the c-axis crystallinity of the AlScN thin films as indicated by the full-width-half-max (FWHM) of the rocking curves increasing. This work provides an analysis of the evolving chemical response of the film elements as Sc target power is changed and underscores the critical role of Sc target power in tuning both composition and structural quality in AlScN thin films.

2.2 Objective & Hypothesis

Dual target co-sputtering with an AlN and Sc metal target provides the capability to tune Sc concentrations (up to 27 at %) in the wurtzite AlScN solid-solution through the adjustment of the Sc target power between 100 – 150 W, chemical analyses reveals the presence of the Sc-N and Al-N chemical states along with oxynitride bonding and evolving surface morphologies related to Sc target power.

The objective of the work proposed in this section is to:

1. Develop a processing route to deposit AlScN with > 20 at % Sc

2. Investigate the impact of increasing Sc target power on the Sc concentration and the respective chemical states of the constituent film elements

3. Observe any structural changes that come about as the Sc target power is increased

2.3 Introduction

Aluminum nitride (AlN) is a wide band gap semiconductor material (E_g> 6.2 eV)[4], with a piezoelectric response that is stable above 1000°C.[4] AlN has previously been developed for piezoelectric applications such as in micro-electromechanical systems (MEMS) [3], acoustic wave filters for RF communication[3], and energy harvesters.[4] The piezoelectric properties of AlN stem from its polar wurtzite crystal structure ($P6_3mc$ space group) where the spontaneous polarization is along the polar hexagonal axis (c-axis).[5,7] The non-centrosymmetric nature of the wurtzite structures gives rise to a d_{33} piezoelectric coefficient of 4.1 pm / V (where d_{33} is defined as the charge generated per unit stress along the same axis as the applied force),[5] and an effective electromechanical coupling coefficient ($k_{t,eff}^2$) of 6.5% (where k quantifies the efficiency of energy conversion between electrical and mechanical domains in piezoelectric materials).[1] Doping AlN with Sc has been shown to enhance the piezoelectric coefficient by up to 400%.[11,15] While both elements share the +3-valence state, the Sc ion has a larger ionic radius than Al, which lengthens and increases the ionicity of the bond with N, as compared to the undoped AlN.[4,8] The increase in piezoelectric response has previously been attributed to the effective softening of the metal-nitrogen bond.[4,8] An additional benefit of doping with Sc is that AlScN retains the wide band gap and chemical and temperature stability inherent to AlN.

To exhibit a macroscopic piezoelectric response along the film thickness, AlScN thin films must consist predominantly of crystallites with their c-axis oriented perpendicular to the substrate surface, as the piezoelectric response arises along this axis in its non-centrosymmetric wurtzite structure. To template the alignment of a thin film along a desired crystallographic axis during deposition, it is common to use a seed or template layer which has lattice parameters within a 5% lattice match or less.[7,16] For AlScN thin films, hexagonal seed layers, such as AlN, Mo, or W[16] are often used as bottom electrodes to promote (0002) texture.. However, the drive to integrate AlScN directly into CMOS necessitates understanding the microstructural evolution and resulting performance for films deposited onto non-lattice matched substrates such as silicon or silicon oxide. The direct growth of c-axis oriented AlScN on Si without a seed layer presents several challenges, primarily due to the greater than 40% lattice mismatch as Si provides no structural guidance for the AlScN film.[17]

While AlScN films with Sc concentrations < 20 at.% have been deposited on (100) Si substrates, achieving films with higher Sc content and exclusive c-axis orientation is still a difficult challenge.[4,15,18] Previous studies have shown Sc sputtering target power influences, not just the Sc concentration, but also impurity concentrations (primarily oxygen inclusion[19,20]and secondary phases[19–21]) of the resultant co-sputtered films. Recent studies have shown that increased Sc concentrations in the film brings about an increase in surface and bulk oxygen, in part due to Sc's high affinity for oxygen.[19,20] Oxygen impurities can reduce c-axis texture by introducing oxynitride bonding or oxygen related secondary phases that decrease c-axis crystallinity.[21,22] Investigating the effects of increasing Sc sputtering target power on atomic bonding provides insights into Sc incorporation and oxygen impurity inclusions (as oxynitride phases or oxide secondary phases, such as Sc-O) at higher Sc concentrations. Notably, oxygen concentrations as high as 28 at % [19,23] have been found in AlScN films with 26 at % Sc even when grown at pressures below 10^{-7} Torr.[19,23,24] While prior studies have not thoroughly examined the chemical states of the oxygen impurities, the presence of such high oxygen concentrations suggests additional oxidation pathways that warrant further investigation. [19,23,24] Since target impurities alone cannot account for 28 at % oxygen incorporation, it is essential to analyze the specific chemical states of the Al, Sc, N, and O present. Understanding the structural and chemical variations as Sc sputtering target power is increased is critical for elucidating how Sc incorporates into the Al-N lattice.

This study characterizes the impact of increasing Sc target power on the composition and microstructure of AlScN films deposited onto SiO_2-Si substrates. The films are deposited via a DC/RF co-sputtering process with a ceramic AlN target and a metal Sc target, where the Sc target power is increased incrementally from 100 – 150 W (33 – 50 % target power relative to the AlN target power). The resulting AlScN films exhibit Sc concentrations ranging from 17 at % to 27 at % . The impact of Sc target power on the phase and crystallographic orientation is determined by X-ray diffraction (XRD). The composition and chemical states of the constituent film elements and impurities are measured through X-ray photoelectron spectroscopy (XPS), and the evolving surface structure and morphology are investigated using atomic force microscopy (AFM) and scanning electron microscopy (SEM).

2.4 Experimental Methods

AlScN thin films were sputter deposited in a dedicated nitride chamber (AJA International Orion Series Sputtering System) onto (100) silicon wafers (MTI Corporation). Prior to deposition the wafers were cleaned in three subsequent cleaning processes by ultrasonication: first in acetone, followed by isopropyl alcohol, and then deionized water for three minutes each. The AlScN thin films were deposited from two discrete targets (2N purity, Kurt J Lesker) concurrently: AlN (RF source) and Sc metal (DC source). DC and RF sputtering were conducted simultaneously from an Sc and AlN target, respectively, to controllably vary the Sc concentration in the $Al_xSc_{1-x}N$ films. The power of the AlN sputter target was held constant at 300 W for all depositions while the Sc target power was varied from 100 W, 125 W, and 150 W. All films were grown using a constant gas flow of 43 sccm with a 2:1 ratio of N_2:Ar. The base chamber pressure prior to deposition was < 7.0×10^{-8} Torr. The substrate temperature was held constant at 300 °C for all depositions. The temperature and partial pressures were chosen to be consistent with previous reports on the sputter deposition of AlScN.[4,7–9]

The phase and crystallographic orientation of the AlScN thin films were determined via XRD on a Rigaku SmartLab XE system using a Cu Kα source (λ = 1.540 Å) operated at 40 kV and 44 mA. All XRD scans employed a 0.01° step size and a scan rate of 2° per minute at room temperature using a Ge (220) monochromator. Rocking curve measurements were performed using a 0.01° step size along with a scan rate of 1° per minute. The film thickness was determined by profilometry which was performed with a Veeco Dektak 150 series Surface Profilometer where a stylus with a 2.00 mg force and a

0.167 mm resolution was used to track step height to determine both film thickness and etch profile depth.

The chemical composition of the films was determined through X-ray photoelectron spectroscopy (XPS). The XPS analysis was conducted ex-situ so the films were exposed to atmosphere between the deposition and transfer to the XPS analysis chamber. The XPS experiments were performed using a Thermo K Alpha XPS system that has an energy range of 100 – 4000 eV and utilizes a dual-beam Al Kα source and a micro-focused monochromator. A flood gun was used to minimize surface charging during scanning and depth profiling. To compensate for any further charging the adventitious carbon (C) 1s peak was set to 284.8 eV according to reference.[25,26] XPS scans were taken before and after etching to determine the bulk film composition and the presence of surface oxidation. Ion etching during XPS was performed using an argon (Ar) ion beam (3000 eV ion energy) in 20 individual etch segments, with each segment lasting for 5 seconds. Scans were taken between each etch segment; a wait period of 60 seconds after the end of etching was used before the scan was taken to form a depth profile. The post-etch XPS scans consist of two survey scans through the entire eV range, followed by 10 individual scans of each of the individual elements (Al 2p, N 1s, Sc 2p, C 1s, O 1s). For XPS scans taken after etching, where the adventitious carbon peak was absent, the charge corrected pre-etch N 1s peak was used as a reference peak. The base pressure of the XPS system was below $1x10^{-7}$ Torr for the evacuation of the etched species. Analysis of the XPS data was conducted using the Avantage software (version 5.9925) for peak fitting and multivariate analysis, from which the film stoichiometry and individual elemental percentages within the film were determined. The peak spacing for the Sc doublets was kept consistent as the peak spacing of the doublet is based on the spin-orbit coupling in this orbital.[27,28] The full width at half max (FWHM) for the fitted peak width is limited from 0.5 – 3.0 and the chi-squared value is kept below 2 to be consistent with common XPS fitting procedures.[26,27,29]

The grain size of the deposited AlScN thin films was determined from SEM and the surface morphology was characterized from AFM images. The SEM imaging was performed using a Hitachi SU8010 SEM (5 kV accelerating voltage, 6.4 mm working distance). The grain size was determined by using a standard contrasting and fitting procedure in ImageJ.[30] The surface morphology was further characterized using tapping mode AFM on a Bruker Icon Scanning using a Scanasyst Air (Bruker) tip (2 kHz peak force frequency, 256 cans per line, 0.4 N/m force).[31]

2.5 Results & Discussion

To determine the impact of varying the scandium target power on the amount of Sc incorporated into the AlScN thin films, XPS spectra were taken for films deposited with varying Sc target power. XPS provides information about the chemical composition and bonding configuration of the elements in a material. **Figure 1a** depicts the fitted post-etch scans of the Sc 2p and the N 1s spectra. **Figure 1b and 1c** depict the same post-etch spectra for the 125 and 150 W films, respectively. An etch was conducted to remove the surface oxide in order to determine the bulk composition of the films. The data in **Figure 1** was collected after etching to a depth of approximately 30 nm into the film with a prescribed wait period of 60 seconds between etching and scanning to minimize redeposition of the etched species.

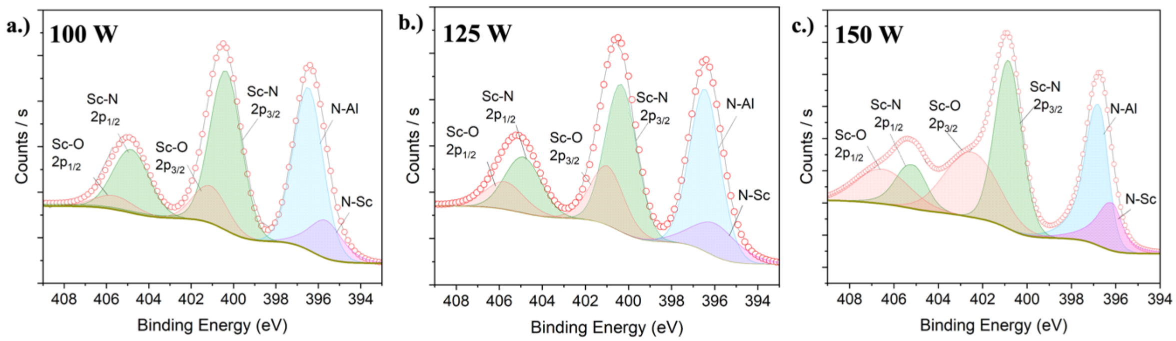

Figure 1. **(a.)** The XPS data of the Sc 2p and N 1s peaks for an AlScN film deposited with 100 W Sc power; **(b.)** The Sc 2p and N1s peaks for an AlScN film deposited with125 W Sc power; **(c.)** The Sc 2p and N 1s peaks for an AlScN film deposited with 150 W Sc power

The Sc 2p spectra, shown in **Figure 1**, can be deconvoluted into two doublets, which are attributed to Sc-N [27] and Sc-O [29] respectively – demonstrating that Sc is bonded to nitrogen, with some oxynitride present. For the films grown at 100 and 125 W Sc target power, the positions of the Sc-N 2p 1/2 and 3/2 doublet peaks are centered about 401.1 and 405.3 eV, which are consistent with the peak positions reported in literature.[27–29,32] The peak spacing for the Sc doublets was held constant during fitting at 4.5 eV on the basis of the expected spin-orbit coupling.[27,32]

The center of the Sc-N 2p doublet peaks for the 150 W Sc films are shifted to 401.8 and 405.6 eV. While the centroid of the overall envelope changes due to the increased Sc-O contributions (demonstrated by the increased FWHM of the envelope and Sc-O peak), the nitride peak itself should not shift relative to the oxide peak. The observed change in the nitride peak likely occurs due to the formation of an oxynitride or an undercoordination of Sc.[27,33]

Additionally, the Sc-O peak's FWHM, in the 150 W films, is 45 % greater than the observed FWHM of the 100 and 125 W films. The Sc-O 2p 3/2 and 1/2 peaks can be seen as clear shoulders in the 150 W films and have FWHM of 2.82 eV. There is no discernable peak centered at 398.6 eV - the typical binding eV for Sc metal.[22] Overall, as the Sc power is increased from 100 to 150 W, the Sc concentration in the films increases from 16.8 to 26.5 at.%. Associated with the change in Sc concentration is a consistent decrease in the Al concentration which suggests that Sc is substituting for Al on the same sub-lattice.

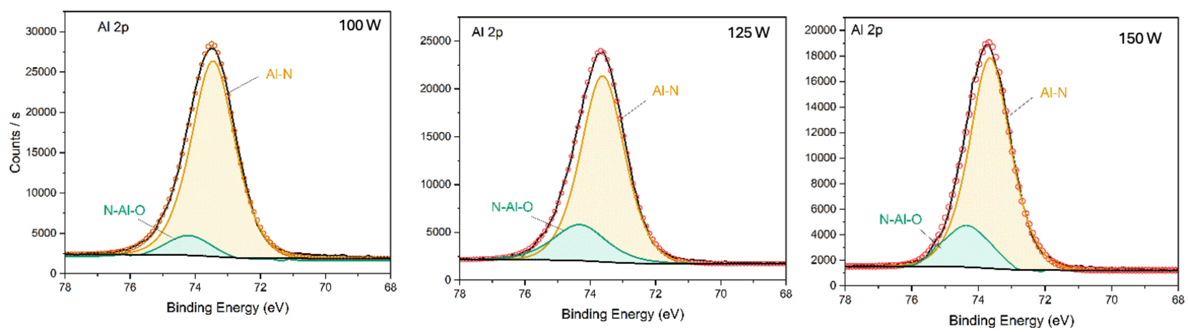

Figure 2. (a.) XPS data of the Al 2p peak for an AlScN film deposited with 100 W Sc power; **(b.)** The Sc 2p peak for an AlScN film deposited with125 W Sc power; **(c.)** The Al 2p peak for an AlScN film deposited with 150 W Sc power

Figure 2 presents the Al 2p spectra, where there are two peaks centered at 73.5 ± 0.2 eV and 74.3 ± 0.2 eV for all films. The Al-N binding energies lie within the literature range from 73.5 eV [34,35] to 74.70 eV. [29,36] Previous reports reference the peak at 73.5 eV as belonging to Al-N [29,36,37], with the higher binding eV peak being assigned to Al-O.[29,36,38] The decrease of the Al spectra further supports the scandium spectra fits showing that Sc is primarily integrating into the AlN matrix rather than forming chemically distinct Sc rich secondary phases, which would not result in a corresponding decrease in Al concentration.

Table 1 provides a synopsis of how the Sc and Al concentrations vary with Sc target power. The composition of the films is determined from the post-etch scans, given that Al and Sc have a propensity to form surface oxide layers.[14,39] The values reported in **Table 1** represent the average film stoichiometry in at.% for 10 separate scans taken after an etch time of 100 s. The etch profile described leads to an average scan depth of ~160 – 170 nm in the film bulk, as measured by profilometry. Overall, the fitted XPS results show that increasing the Sc target power leads to an increase in the Sc concentration in the films with concomitant decrease in Al.

Table 1. Summary of the atomic percentages of the constituent elements (Sc, Al, N, O, and C) from the AlScN thin films grown at different Sc target powers

Sc Target Power (W)	**Scandium (at %)**	**Aluminum (at %)**	**Nitrogen (at %)**	**Oxygen (at %)**	**Carbon (at %)**
100	**16.8**	**30.9**	**36.8**	**15.5**	**-**
125	**21.4**	**25.7**	**30.3**	**20.3**	**2.2**
150	**26.5**	**21.6**	**27.7**	**20.9**	**3.1**

Table 1 also shows the atomic percentages of nitrogen and oxygen in the bulk of the AlScN thin films. The N 1s profile, which is visible in **Figure 1**, is deconvoluted into two peaks for all films which are attributed to the bonding with Sc-N and Al-N. The peak at 396.6 ± 0.1 eV fits within the range of reported literature values (396.4 – 397.9 eV) [38-36] for the N 1s peak associated with the Al-N bond in the wurtzite structure. The second peak at 395.7 ± 0.2 eV is attributed to the Sc-N bond,[22] which further supports the incorporation of Sc into the film.

However, nitrogen is not the only anion species observed in these films. The XPS results also provide insight into the presence of oxygen throughout the depth of the post-etched films. **Figure 3** depicts the XPS response in the region of binding energies associated with oxygen. The films are predominantly nitrides, and thus the local bonding configuration is likely oxynitride. However, there are still features associated with Al_2O_3 and Sc_2O_3 - the anticipated compositions for fully oxidized aluminum and scandium. The characteristic oxygen peak associated with Al_2O_3 is found at 531 ± 0.7 eV, and the peak at 529 ± 0.2 eV has previously been attributed to Sc_2O_3.[40,41] From the analysis of the post-etch peaks at 531 and 529 eV, the bulk oxygen concentrations are 15.5, 20.3, and 20.9 at.% for the 100, 125, and 150 W Sc target power films respectively. It is likely that the amount of oxygen is overestimated, as previous studies have shown the redeposition of oxygen during Ar^+ ion etching in XPS conditions that are analogous to this work.[24,26] However, the oxygen concentration throughout the thickness of the films remains higher than would be expected from solely redeposition. There is a change in peak profile and position upon entering the bulk of the film after ~10 nm of etching, that indicates that the local coordination of the oxygen has changed from predominantly oxide towards a mixed oxynitride configuration.

Prior to etching, the surface oxide accounts for 33.0, 25.9, and 26.3 at.% in films grown at 100, 125, and 150 W Sc target powers, respectively. The bulk oxygen concentrations are found to be 15.5, 20.3, and 20.9 at.% for the respective 100, 125, and 150 W Sc target power films. Increasing the Sc target power leads to higher percentages of oxygen in the post-etch spectra. Given that the base pressures of the sputtering chamber was held constant for all film depositions (< 7.0×10^{-8} Torr), and the pressure of the XPS system was also held constant (< 3.0×10^{-7} Torr) , the relative difference in oxygen concentrations in the films must stem from either a difference in the deposition conditions or from differences in the incorporated oxygen due to variations in the resulting microstructure. From the impurity analysis of the Sc target, a maximum of 2.2 at % oxygen incorporation would be expected, which would lead to an increase from 1.4 at % to 2.2 at % oxygen upon going from 100 W to 150 W.

Previous studies of AlScN thin film deposition have identified up to 28 at.% oxygen in films with 26 at.% Sc.[19]. Sc exhibits a strong propensity to oxidize, but the 5-minute pre-sputter, described in the method section, of the target is anticipated to have removed much of the surface oxide from the Sc target prior to deposition. Additionally, although target power has been shown to change the deposition energetics (i.e. – kinetic energy and flux of sputtered species, adatom energies, etc.) [42,43] and the incorporation of atoms from the processing atmosphere into the thin film,[7,42] depositing in ultra-high purity nitrogen would not have permitted oxygen incorporation at the levels observed in this study. Therefore, variations in Sc target power can only account for 0.8 at.% of the incorporated oxygen. The remaining bulk oxygen incorporation (> 15 at %) is likely due to differences in microstructure (which will be described in a latter section), including the deeply grooved grain boundaries of the faceted grains that allow for oxygen permeation into the bulk and grain boundaries density, leading to differences in the absorption of oxygen once the films were exposed to atmosphere.

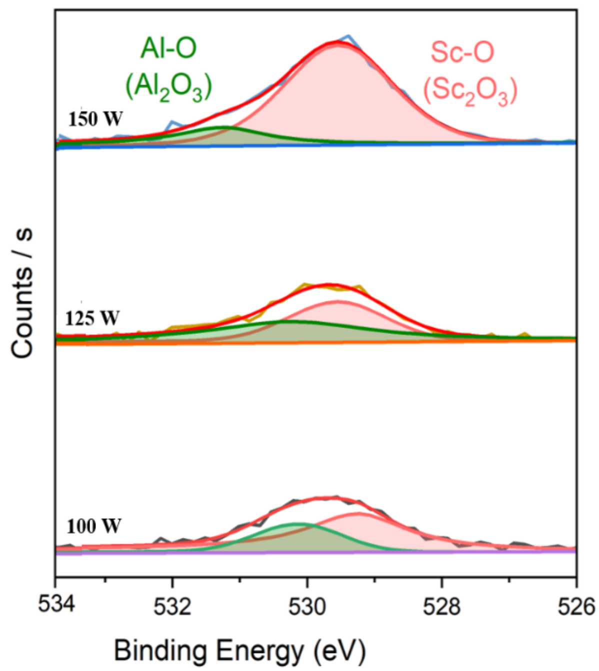

Figure 3. XPS spectra of the post-etch oxygen spectra for all films with increasing Sc target power as the graph ascends

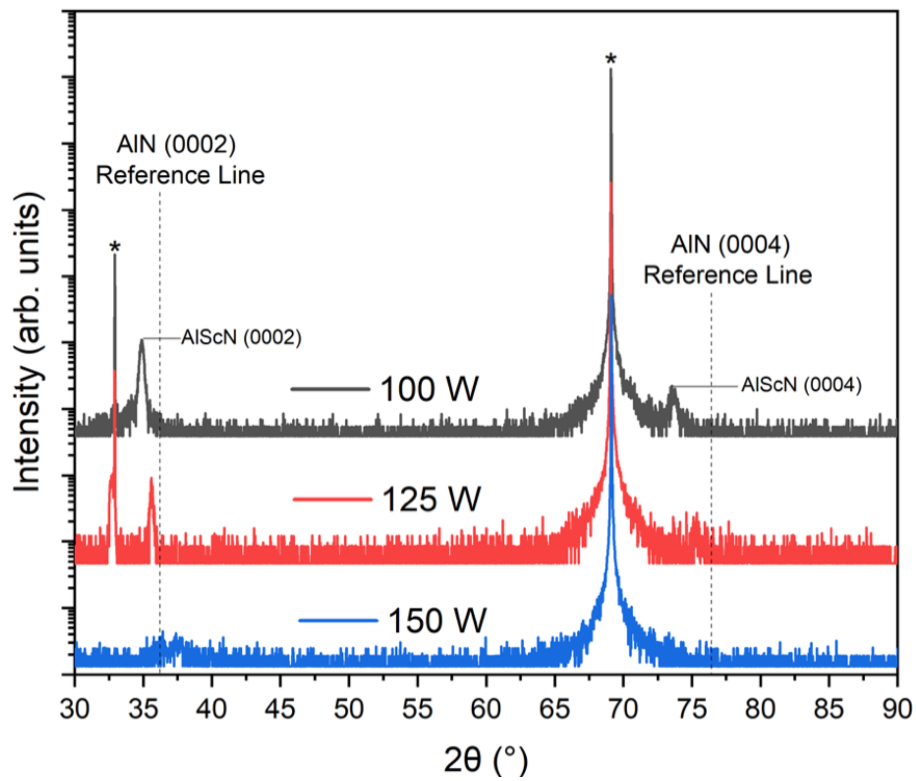

Figure 44. XRD of AlScN thin films grown at different Sc target powers. The starred peaks represent the Si related substrate peaks

XRD 2θ scans show the impact of Sc target power on the phase and crystallographic alignment of the resultant AlScN thin films when grown on (100) Si. **Figure 4** shows the XRD data for films grown at 100, 125, and 150 W Sc target powers. Films deposited at 100 W and 125 W have diffraction peaks that correspond to a (0002) oriented wurtzite type structure with a ($P6_3mc$) hexagonal phase. The (0002) peaks are an indication of c-axis texture - or growth in the c-axis direction of the wurtzite phase. The observed AlScN (0002) and (0004) reflections are presented in **Figure 4** along with the wurtzite AlN reference peaks (CIF number: 01-070-2545) represented as dashed lines [33] - the diffraction peaks shift away from the AlN reference indicates Sc incorporation in the AlN matrix. The shift in the (0002) peaks away from the expected AlN reflection at 36.04°, for all the presented AlScN films, indicates a change in the d-spacing, which suggests Sc incorporation within the films as a negative shift in 2q is expected due to the larger Sc ion increasing the lattice parameters.[12] The expected 2θ values for the AlScN films with a measured Sc concentration of 17 and 21 at %, are calculated to be 35.76° and 35.72° respectively, using Vegard's Law on the basis of a solid solution between the endmember AlN – ScN that maintains a consistent hexagonal phase.[34] The calculated 2q values lead to the theoretical out-of-plane lattice parameter (c-lattice parameter) constants of 5.018 Å and 5.023Å. The experimentally observed (0002) and (0004) diffraction peaks for the films grown at 100 and 125 W Sc target power, show a decrease in their 2q angle with respect to the reference AlN peak and have an average out-of-plane lattice parameters of 5.01 Å and 4.97 Å for the 17 and 21 at % films respectively. Thus, the average shift in 2q found in the experimental XRD analysis supports the observed concentrations found in the 100 and 125 W films as determined by XPS. The experimental c-lattice parameters are within a 10 % of the theoretical out-of-plane c-lattice constants found using the described Vegard's Law. [34] The experimental c-lattice parameters are reported in **Table 2** and are in agreement with literature, where the c-lattice parameters of the wurtzite AlScN films at their respective measured Sc concentrations (17 and 21 at.% Sc), should be approximately 5.0 to 4.96 Å respectively. [12,35]

When the Sc target power is increased to 150 W, there is a reduction in the intensity of the wurtzite phase (0002) peak, as seen in the blue diffraction pattern in **Figure 4**. The peak broadening of the (0002) reflection suggests reduced c-axis crystallite coherence. There are reports of the peak intensity of the AlN (0002) [36,37] and AlScN (0002) [38] reflections gradually decreasing with increasing oxygen concentration, which matches the XPS trends seen in **Figures 2 and 3**. The 150 W films have limited c-axis texture - or growth in the c-axis direction - as seen in the reduced wurtzite diffraction peak intensities in **Figure 4**; as demonstrated in the XPS measurements presented in **Figures 1** and **2**.

The 150 W films exhibit a (0002) diffraction peak at 36.72° in 2θ, leading to a c-lattice parameter of 4.95 Å, and continues the trend of decreasing c-lattice parameter with increasing Sc target power. The observed lattice parameter of 4.95 Å for the 150 W films are comparable to films reporting > 38 at % Sc concentration, [12] which does not align with the measured Sc concentration of 27 at % found in the XPS measurements. Amorphous oxygen phases have been previously shown to increase in-film strain leading to increases in the 2q angle of AlScN thin films grown under similar conditions. [38,39] However, the intensity of the further peak reflections past the (0002) reflection in the (*0002l*) family (2*l* = [2,4,8]) are not above the baseline system counts and cannot be used to further probe peak strain. Overall, the presence of the wurtzite diffraction peaks in films deposited under all conditions demonstrates that c-axis textured can be induced in AlScN without a seed layer.

Table 2. A summary of compositional, crystallographic, and morphological information as a function of Sc target deposition powers

Scandium Target Power (W)	Film Composition	c - Lattice Parameter (Angstroms)	Grain Size (nm)	Rocking Curve FWHM (°)	Surface Roughness (nm)
100	$Al_{0.31}Sc_{0.17}N_{0.37}O_{0.15}$	5.01	26 ± 3	2.67	1.3
125	$Al_{0.26}Sc_{0.21}N_{0.31}O_{0.20}C_{0.02}$	4.97	31 ± 1	3.01	2.6
150	$Al_{0.23}Sc_{0.27}N_{0.27}O_{0.2}C_{0.03}$	4.95	33 ± 1	-	4.2

Rocking curve (RC) measurements provide information on the orientation distribution of crystal lattice planes (the mosaic spread of the crystallites in the sample) by scanning around the ω axis of a particular reflection found in the 2θ scan.[40] The peak width, or the full width at half maximum (FWHM), of the RC measurement is dependent upon the mosaic spread of crystallites, the dislocation density in the sample, and the curvature of the substrate – all of which will influence the parallel nature of the lattice planes.[40] Therefore, RC measurements are used as a general indication of the quality of a crystalline film and an indication of preferential orientation.[40] RC measurements are performed on all films (100 ,125, and 150 W films); these results are summarized in **Table 2**. The RCs reveal that the films deposited at 100 and 125 W Sc have FWHM values of 2.67° and 3.01°, respectively. The measured FWHM of the peak for the 150 W samples is ~16°.

The RC FWHM values, shown in table 2, indicate that as Sc target power increases, the crystalline orientation of the films decreases. The decreasing crystalline coherence can be observed in the 2θ scans as well (**Figure 3**), where the intensity of the (0002) and (0004) reflections decrease with increasing Sc target power. The trend of an increasing FWHM with higher Sc concentrations is consistent with literature.[12,35,41] Additionally, oxygen impurities at 5 at % have been shown to decrease the coherence of crystallographic alignment and increase the RC FWHM to as much as 12° in AlN systems grown directly on (100) Si.[36]

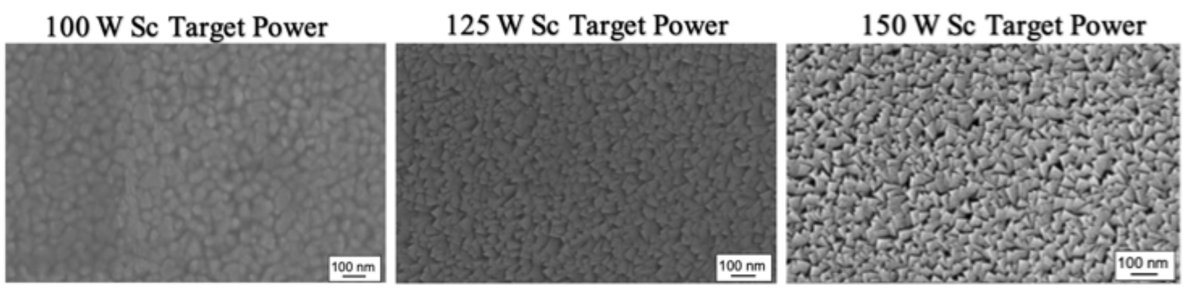

Figure 5. SEM micrographs of (a.) 100, (b.) 125, and (c.) 150 W Sc target power film

Reduced surface roughness is critical in the development of MEMS and RF devices as this reduces the likelihood of acoustic and electrical scattering. [51,52] From this perspective, and smooth surfaces with minimal roughness are preferred. [51,52] The surface morphology and grain structure of the films are characterized and shown in SEM micrographs in **Figures 5a** (100 W), **5b** (125 W), and **5c** (150 W Sc target power). The grain size at the film surface, reported in **Table 2**, is found to increase with increasing Sc content, from 26 ± 3 to 33 ± 1 nm as Sc target power is increased from 100 – 150 W. In AlScN thin films with grains below 40 nm, grain boundaries exacerbate bulk oxygen and carbon incorporation by serving as percolation pathways into the film. [20,32,52] The films in this study have grains smaller than 40 nm, making them susceptible to oxygen infiltration, which is likely the dominant mechanism for the incorporation of oxygen into the films with Sc concentrations greater than 21 at %. AFM analysis further supports the morphology findings from SEM. The AFM reveals a steady increase in the average surface roughness (Ra) from 1.3 nm (100 W) to 4.2 nm (150 W) with increasing Sc target power and follows a similar trend as the increasing RC FWHM. The increased surface roughness stems from the appearance of triangular surface facets, as shown in **Figures 4b** and **4c**. Films grown at 100 W Sc target power had a surface morphology with no triangular facets observed. The 125 W Sc target power has a surface that is dominated by surface facets, which increases the surface roughness and creates a surface that would lead to a less efficient device with increased losses. Thus, the progressive increase in Sc target power enhances grain size but also introduces morphological changes – specifically, increased surface roughness and triangular facets, that compromise the film's suitability for device integration by promoting uncontrolled oxygen infiltration and by increasing potential scattering losses in device operation.

2.6 Conclusions

This study demonstrates the direct growth of AlScN thin films without a seed layer. Clear (0002) and (0004) diffraction peaks are observed in XRD for films containing less than 21 at.% Sc. Surface facets are observed on films grown at 125 and 150 W and the appearance of the facets coincide with a decrease in the intensity of the (0002) and (0004) reflections. XPS shows that there is an increasing scandium concentration from 21 to 27 at % Sc when increasing the Sc target power from 100 W to 150 W. Additionally, increased oxygen incorporation from 15 to 21 at % is also observed with increasing Sc target power. By systematically investigating the impact of Sc sputtering target power on the film composition, surface structure, crystallinity, and oxidation, this study identifies a trade-offs between increased Sc content and structural degradation for AlScN thin films.

2.7 References

1. Wellington-Johnson, J., Frye, M., Chuong, K., Graham, I. & Osterholm, A. Impact of scandium target power on the microstructure and chemical response of co-sputtered Al1-xScxN thin films grown on (100) Si. *Journal of Vacuum Science & Technology B*.
2. Sekhar, M. C. *et al.* A Review on Piezoelectric Materials and Their Applications. *Crystal Research and Technology* **58**, 2200130 (2023).
3. Chen, L. *et al.* Scandium-Doped Aluminum Nitride for Acoustic Wave Resonators, Filters, and Ferroelectric Memory Applications. *ACS Appl. Electron. Mater.* **5**, 612–622 (2023).
4. Zhang, Y., Zhu, Q., Tian, B. & Duan, C. New-Generation Ferroelectric AlScN Materials. *Nanomicro Lett* **16**, 227 (2024).
5. Pinto, R. M. R., Gund, V., Dias, R. A., Nagaraja, K. K. & Vinayakumar, K. B. CMOS-Integrated Aluminum Nitride MEMS: A Review. *Journal of Microelectromechanical Systems* **31**, 500–523 (2022).

6. Mikolajick, T. *et al.* Next generation ferroelectric materials for semiconductor process integration and their applications. *Journal of Applied Physics* **129**, 100901 (2021).
7. Iriarte, G. F., Rodríguez, J. G. & Calle, F. Synthesis of *c*-axis oriented AlN thin films on different substrates: A review. *Materials Research Bulletin* **45**, 1039–1045 (2010).
8. Satoh, S., Ohtaka, K., Shimatsu, T. & Tanaka, S. Crystal structure deformation and phase transition of AlScN thin films in whole Sc concentration range. *Journal of Applied Physics* **132**, 025103 (2022).
9. Österlund, E. *et al.* Stability and residual stresses of sputtered wurtzite AlScN thin films. *Phys. Rev. Materials* **5**, 035001 (2021).
10. Deng, R., Jiang, K. & Gall, D. Optical phonon modes in Al1−xScxN. *Journal of Applied Physics* **115**, 013506 (2014).
11. Akiyama, M. *et al.* Enhancement of Piezoelectric Response in Scandium Aluminum Nitride Alloy Thin Films Prepared by Dual Reactive Cosputtering. *Advanced Materials* **21**, 593–596 (2009).
12. Fichtner, S., Wolff, N., Lofink, F., Kienle, L. & Wagner, B. AlScN: A III-V semiconductor based ferroelectric. *Journal of Applied Physics* **125**, 114103 (2019).
13. Hackett, L. *et al.* Aluminum scandium nitride films for piezoelectric transduction into silicon at gigahertz frequencies. *Applied Physics Letters* **123**, 073502 (2023).

14. Zywitzki, O., Modes, T., Barth, S., Bartzsch, H. & Frach, P. Effect of scandium content on structure and piezoelectric properties of AlScN films deposited by reactive pulse magnetron sputtering. *Surface and Coatings Technology* **309**, 417–422 (2017).

15. Beaucejour, R. *et al.* Controlling Residual Stress and Suppression of Anomalous Grains in Aluminum Scandium Nitride Films Grown Directly on Silicon. *Journal of Microelectromechanical Systems* **31**, 604–611 (2022).

16. Su, J. *et al.* Growth of Highly c-Axis Oriented AlScN Films on Commercial Substrates. *Micromachines* **13**, 783 (2022).

17. Full article: Thermal conductivity enhancement of aluminum scandium nitride grown by molecular beam epitaxy. https://www.tandfonline.com/doi/full/10.1080/21663831.2023.2279667.

18. Qin, H. *et al.* Perspectives of Ferroelectric Wurtzite AlScN: Material Characteristics, Preparation, and Applications in Advanced Memory Devices. *Nanomaterials (Basel)* **14**, 986 (2024).

19. Casamento, J., Xing, H. G. & Jena, D. Oxygen Incorporation in the Molecular Beam Epitaxy Growth of ScGa1−N and ScAl1−N. *physica status solidi (b)* **257**, 1900612 (2020).

20. Li, M., Hu, K., Lin, H., Felmetsger, V. & Zhu, Y. Oxidation of sputtered AlScN films exposed to the atmosphere. in *2022 IEEE International Ultrasonics Symposium (IUS)* 1–3 (2022). doi:10.1109/IUS54386.2022.9957694.

21. Akiyama, M., Kamohara, T., Kano, K., Teshigahara, A. & Kawahara, N. Influence of oxygen concentration in sputtering gas on piezoelectric response of aluminum nitride thin films. *Applied Physics Letters* **93**, 021903 (2008).

22. Wang, M. *et al*. High-quality c-axis oriented Al(Sc)N thin films prepared by magnetron sputtering. *Thin Solid Films* **781**, 140000 (2023).

23. Lee, C.-W., Din, N. U., Brennecka, G. L. & Gorai, P. Defects and oxygen impurities in ferroelectric wurtzite Al1−xScxN alloys. *Applied Physics Letters* **125**, 022901 (2024).

24. Li, M., Lin, H., Hu, K. & Zhu, Y. Oxide overlayer formation on sputtered ScAlN film exposed to air. *Applied Physics Letters* **121**, 111602 (2022).

25. Biesinger, M. C. Accessing the robustness of adventitious carbon for charge referencing (correction) purposes in XPS analysis: Insights from a multi-user facility data review. *Applied Surface Science* **597**, 153681 (2022).

26. Greczynski, G. & Hultman, L. A step-by-step guide to perform x-ray photoelectron spectroscopy. *Journal of Applied Physics* **132**, 011101 (2022).

27. Biesinger, M. C., Lau, L. W. M., Gerson, A. R. & Smart, R. St. C. Resolving surface chemical states in XPS analysis of first row transition metals, oxides and hydroxides: Sc, Ti, V, Cu and Zn. *Applied Surface Science* **257**, 887–898 (2010).

28. Haasch, R. T., Lee, T.-Y., Gall, D., Greene, J. E. & Petrov, I. Epitaxial ScN(001) Grown and Analyzed In situ by XPS and UPS. I. Analysis of As-deposited Layers. *Surface Science Spectra* **7**, 169–177 (2000).

29. Ding, Y. *et al.* Ultrathin Pt and Mo films on Al1–Sc N: an interface investigation. *Applied Surface Science* **637**, 157921 (2023).

30. Igathinathane, C., Pordesimo, L. O., Columbus, E. P., Batchelor, W. D. & Methuku, S. R. Shape identification and particles size distribution from basic shape parameters using ImageJ. *Computers and Electronics in Agriculture* **63**, 168–182 (2008).

31. Lu, Y. *et al.* Surface Morphology and Microstructure of Pulsed DC Magnetron Sputtered Piezoelectric AlN and AlScN Thin Films. *Physica Status Solidi (a)* **215**, 1700559 (2018).

32. Cohen, A. *et al.* Local Environment of Sc and Y Dopant Ions in Aluminum Nitride Thin Films. *ACS Appl. Electron. Mater.* **6**, 853–861 (2024).

33. Environmental stability and ageing of ScN thin films from XPS Ar+ depth profiling. http://ouci.dntb.gov.ua/en/works/4M0XzJN7/.

34. Alevli, M., Ozgit, C., Donmez, I. & Biyikli, N. Structural properties of AlN films deposited by plasma-enhanced atomic layer deposition at different growth temperatures. *physica status solidi (a)* **209**, 266–271 (2012).

35. Madhuri, A., Jena, S., Gupta, M. & Swain, B. P. Nitrogen flow rate dependent atomic coordination, phonon vibration and surface analysis of DC magnetron sputtered nitrogen rich-AlN thin films. *Physica B: Condensed Matter* **666**, 415141 (2023).

36. Motamedi, P. & Cadien, K. XPS analysis of AlN thin films deposited by plasma enhanced atomic layer deposition. *Applied Surface Science* **315**, 104–109 (2014).

37. Wang, W. B. *et al.* AlScN thin film based surface acoustic wave devices with enhanced microfluidic performance. *J. Micromech. Microeng.* **26**, 075006 (2016).

38. Sharma, N., Ilango, S., Dash, S. & Tyagi, A. K. X-ray photoelectron spectroscopy studies on AlN thin films grown by ion beam sputtering in reactive assistance of N+/N2+ ions: Substrate temperature induced compositional variations. *Thin Solid Films* **636**, 626–633 (2017).

39. Garcıa-Mendez, M., Morales-Rodrıguez, S. & Machorro, R. Characterization of ALN thin films deposited by DC reactive magnetron sputtering. (2008).

40. Liu, A. *et al.* Water-Induced Scandium Oxide Dielectric for Low-Operating Voltage n- and p-Type Metal-Oxide Thin-Film Transistors. *Advanced Functional Materials* **25**, 7180 (2015).

41. Wu, Y. *et al.* High-Surface Area Mesoporous Sc2O3 with Abundant Oxygen Vacancies as New and Advanced Electrocatalyst for Electrochemical Biomass Valorization. *Advanced Materials* **36**, 2311698 (2024).

42. Farhadizadeh, A. & Kozák, T. The importance of discharge voltage in DC magnetron sputtering for energy of sputtered and backscattered atoms on the substrate: Monte-Carlo simulations. *Vacuum* **196**, 110716 (2022).

43. Sigmund, P. Theory of Sputtering. I. Sputtering Yield of Amorphous and Polycrystalline Targets. *Phys. Rev.* **184**, 383–416 (1969).

44. Signore, M. A. *et al.* Effect of silicon-based substrates and deposition type on sputtered AlN thin films: Physical & chemical properties and suitability for piezoelectric device integration. *Applied Surface Science* **599**, 154017 (2022).

45. Urban, D. F., Ambacher, O. & Elsässer, C. First-principles calculation of electroacoustic properties of wurtzite (Al,Sc)N. *Phys. Rev. B* **103**, 115204 (2021).

46. Zhang, X., Stach, E. A., Meng, W. J. & Meng, A. C. Nanoscale compositional segregation in epitaxial AlScN on Si (111). *Nanoscale Horiz.* **8**, 674–684 (2023).

47. Fichtner, S., Reimer, T., Chemnitz, S., Lofink, F. & Wagner, B. Stress controlled pulsed direct current co-sputtered Al1−xScxN as piezoelectric phase for micromechanical sensor applications. *APL Materials* **3**, 116102 (2015).

48. Acharya, S. *et al.* Role of oxygen on structure and piezoelectric properties of ${\mathrm{Al}}_{0.65}{\mathrm{Sc}}_{0.35}\mathrm{N}$ thin films. *Phys. Rev. Appl.* **22**, 044071 (2024).

49. Kim, J., Ahn, H., Kim, S.-J., Kim, J.-Y. & Pee, J.-H. Effect of Residual Oxygen Concentration on the Lattice Parameters of Aluminum Nitride Powder Prepared via Carbothermal Reduction Nitridation Reaction. *Materials* **15**, 8926 (2022).

50. Harrington, G. F. & Santiso, J. Back-to-Basics tutorial: X-ray diffraction of thin films. *J Electroceram* **47**, 141–163 (2021).

51. Tang, J., Niu, D., Yang, Y., Zhou, D. & Yang, C. Preparation of ScAlN films as a function of sputtering atmosphere. *J Mater Sci: Mater Electron* **27**, 4788–4793 (2016).

52. Yamashita, M., Sasaki, Y., Ito, H., Ohsato, H. & Shibata, N. Fabrication of Aluminum Nitride Thin Film and Its Oxidation Behavior. 材料 **55**, 785–789 (2006).

CHAPTER 3. EXPERIMENTAL DETERMINATION OF THE IMPACT OF SPUTTERING MODE ON THE FERROELECTRIC RESPONSE OF ALSCN THIN FILMS

3.1 Abstract

The critical limiting factor for AlScN is not temperature or CMOS integration, like other ferroelectric materials[12], but rather the close proximity of the ferroelectric coercive field (E_C) to the breakdown field (E_{BD})[3,4]. Sputtered AlScN shows clear indications of ferroelectric switching, but further advances into the factors that dictate switching and breakdown are critically needed to reach the full potential of ferroelectric AlScN. This study investigates the impact of the sputter deposition method - either DC sputtering, RF sputtering, or simultaneous RF and DC co-sputtering - on the coercive field, permittivity, and breakdown field of AlScN films. $Al_{0.75}Sc_{0.25}N$ thin films were deposited from ceramic targets onto hafnium bottom electrodes at 400 °C. The ferroelectric response for each film type is determined from polarization-electric field (PE) hysteresis loops, polarization-up-negative-down (PUND) measurements, and dielectric and Rayleigh analysis. The RF sputtered AlScN films show clear indications of ferroelectric switching with an average P_R of 98 μC/cm^2 and an E_C of 4.6 MV/cm, while films deposited by DC sputtering show only linear dielectric behavior. The co-sputtered films exhibit a range of ferroelectric and dielectric behavior, with a clear separation between the coercive and breakdown fields. Thus, sputter depositing using multiple modes concurrently is promoted as a route to increase the separation of the coercive and breakdown fields in AlScN thin films.

.

3.2 Objective & Hypothesis

The performance of AlScN as a ferroelectric material is fundamentally limited by the close proximity of its coercive field (E_C) to the dielectric breakdown field (E_{BD}). While increasing scandium content has been shown to lower the coercive field, it also tends to degrade spontaneous polarization and promote undesirable microstructural features such as abnormally oriented grains (AOGs).[1,2] Alternatively, sputtering methodology itself may serve as a process lever to tailor the ferroelectric response of AlScN without altering its composition. Prior work suggests that deposition method - specifically DC sputtering, RF sputtering, or concurrent RF&DC sputtering - has a significant impact on key ferroelectric metrics including E_C, remnant polarization (P_R), and breakdown strength. However, direct comparisons under tightly controlled deposition conditions are limited, and the mechanisms by which deposition energetics affect ferroelectric switching remain poorly understood.

The objective of the work proposed in this section is to:

1. Evaluate the impact of sputtering method (DC, RF, and RF&DC co-sputtering) on the ferroelectric properties of $Al_{0.75}Sc_{0.25}N$ thin films deposited from stoichiometric ceramic targets.

2. Characterize the resulting electrical behavior—including E_C, P_R, and E_{BD}—through polarization-electric field hysteresis (PE), PUND measurements, and Rayleigh analysis.

3. Identify correlations between deposition energetics and the trade-off between polarization magnitude and the separation of coercive and breakdown fields.

Here we propose to systematically compare AlScN films deposited under otherwise identical conditions using three different sputtering modes, in order to isolate the role of deposition physics in shaping the ferroelectric behavior. The goal is to inform deposition strategies that maximize polarization switching performance while mitigating premature electrical breakdown, thereby enabling more robust ferroelectric functionality in AlScN-based devices

3.3 Introduction

While the remnant polarization of aluminum scandium nitride ($Al_{1-x}Sc_{1x}N$) is typically in the range of ~80-165 μC/cm^2,[7] the performance and long term reliability of AlScN is still limited by the close proximity of the coercive field (E_C) to the breakdown field (E_{BD}).[8] Increasing the scandium content in AlScN has been shown to reduce the coercive field from approximately 8 MV/cm at Sc > 10% and up to less than 2 MV/cm for Sc = 43%.[9–11] However, increasing the scandium concentration also decreases the spontaneous polarization and can increase the propensity of crystallographically misoriented grains.[12,13] Thus, an alternative route to increase the separation between the coercive field and breakdown in AlScN is critically needed in order to enable applications that require ferroelectric switching, such as ferroelectric memory or logic.[14]

Initial work on ferroelectric AlScN has focused on the deposition of films through DC reactive sputtering using metal targets (Al, Sc, or Al-Sc alloys) in a reactive nitrogen atmosphere.[15,16] Alternatively, RF sputtering from a stoichiometric ceramic target is also a viable route for AlScN deposition.[17] While a direct comparison of identical films is difficult, there are clear differences in the coercive and breakdown field trends between films deposited by different sputtering methods. Prior work has shown that RF sputtering reduces the coercive field from 6.5 MV/cm (sub-20 nm $Al_{0.28}Sc_{0.32}N$ by DC co-sputtering from metal targets) to 4.4 – 5.4 MV/cm (250 nm $Al_{0.7}Sc_{0.3}N$ by RF sputtering from a ceramic target). [17,18] In addition, for $Al_{0.7}Sc_{0.3}N$ deposited from metal targets, prior work places the average coercive fields for DC deposited films in the range from 3.4 – 4.5 MV/cm for thicknesses of 50 – 100 nm, compared to coercive fields of 5.3 – 6.3 MV/cm for RF sputtered films of thicknesses of 25 – 40 nm.[19–22] One study has also shown that compared to DC reactive sputtering, using a 50-50 mixture of RF and DC power supply to the Al target reduced the E_C of sputtered $Al_{0.7}Sc_{0.3}N$ from 3.7 MV/cm to 3.4 MV/cm.[20,31,5123] The mechanisms behind the reduction in coercive field were not specified. Additionally, there are differences in the reported breakdown fields for DC and RF films, where the former display a E_{BD} of 6.2 – 8 MV/cm and the latter show a E_{BD} of approximately 6.5 – 7 MV/cm.[19,21,24,25] However, it is challenging to draw conclusions from these studies as the electrical properties of AlScN depend upon many processing parameters such as the film thickness, deposition pressure, chemical composition, etc.[26,27] There is limited study on how the sputtering method directly affects the ferroelectric response of AlScN thin films sputter deposited from a ceramic target, with all other conditions held constant.

This study investigates the impact of the sputter deposition method on the ferroelectric and dielectric response of AlScN thin films. The AlScN films were deposited by either DC, RF, or RF&DC co-sputtering using $Al_{0.75}Sc_{0.25}N$ ceramic targets with all other conditions held constant. Thus, this work isolates the impact of deposition energetics to provide insight into the impact of processing directly on the ferroelectric and dielectric response. The ferroelectric response is characterized by polarization-electric field hysteresis (PE) loops, Positive-Up-Negative-Down (PUND) measurements, and Rayleigh analysis. Overall, there was a clear difference in ferroelectric polarization, coercive field, and breakdown strength of AlScN thin films as a function of the sputtering deposition method employed.

3.4 Experimental Methods

Aluminum scandium nitride thin films were deposited by either DC sputtering, RF sputtering, or simultaneous RF and DC sputtering (AJA Sputter System) from $Al_{0.75}Sc_{0.25}N$ ceramic targets. To differentiate films deposited by different sputtering methods, the terms DC, RF, or [RF&DC] co-sputtered films will be used to specify the film type. The AlScN thin films were deposited onto hafnium bottom electrodes, which were deposited onto Si_3N_4 on Si substrates. For the deposition of the hafnium bottom electrodes, first a titanium adhesion layer was DC sputtered from a Ti target (ACI Alloys) for approximately 5 minutes, followed immediately by the DC sputter deposition of hafnium from a Hf target (ACI Alloys) to reach a layer of approximately 100 nm. Then the AlScN thin films were sputter deposited without breaking vacuum, using a power of 200 W under a gas flow of 40 sccm for Ar and 20 sccm for N_2. The total pressure for the RF&DC co-sputtered film had to be increased to 4 mTorr to ensure that both guns would stay lit, while for the other two film types the pressure was held constant at 3 mTorr. The total deposition time was approximately 19800 seconds, and the temperature of the substrates was 400 °C. Gold top electrodes of various sizes (areas of 3.2 mm^2, 0.8 mm^2, and 0.2 mm^2) were deposited as the top electrical contacts.

The capacitance and dielectric loss of the sputtered films were measured using an E4980A Agilent LCR meter at a frequency of 1 kHz and an AC voltage of 1 V. The reported values were the average of 30 measurements taken from multiple electrodes on each film. The relative permittivity was calculated using the measured capacitance, the electrode areas and the thickness of each film measured using scanning electron microscopy (SEM). SEM cross-section micrographs were obtained from a Hitachi SU 8230 SEM at 5 keV and 15 mA. From the cross-sectional images, the average film thicknesses of each film type are 307 ± 8 nm for DC films, 213 ± 4 nm for RF&DC films, and 265 ± 11 nm for RF films. Ferroelectric measurements were conducted using a Radiant Precision Premier II Ferroelectric Tester. For the polarization-electric field (PE) hysteresis loops, the AlScN devices were driven from the bottom electrode. The PE loops were taken at 100 Hz utilizing progressively increasing voltages starting from 30V until electrical breakdown occurred. The electric field required to switch the polarization (coercive field, E_C) was extracted from the positive x-intercept in the PE loops. The same drive voltages were also used in Positive-Up-Negative-Down (PUND) measurements to compare the results. Each PUND waveform contained a voltage pulse of 1 ms followed by a delay of 1000 ms between pulses in a two up – two down profile. The PUND waveforms can be found in **Figure 9**, and the polarization was measured at each input pulse. The polarization values extracted from PUND measurements, P_{PUND}, were calculated as the difference in polarizations measured at the first and the second pulse. It could also be viewed as the difference between P* and P^ in **Figure 9** (both in the unit of μC/cm^2). Again, the voltages applied were normalized to electric fields using the thickness values measured from SEM cross-section images. To further support the ferroelectric analysis, the Rayleigh response of the films was investigated by recording the AC voltage dependence of the permittivity and dielectric loss at 20 Hz, 1 kHz, 10 kHz, and 100 kHz. The applied electric fields were maintained below approximately one-third of the coercive field, to ensure that these measurements were taken in the sub-switching region. The Rayleigh measurements were taken from 1V_{AC} to 20 V_{AC}, using the same LCR meter mentioned above. The reported values were averaged from 10 runs for each sample. The reversible and irreversible Rayleigh coefficients were extracted from the slope and the intercept of the permittivity versus V_{AC} plots, respectively.

3.5 Results & Discussion

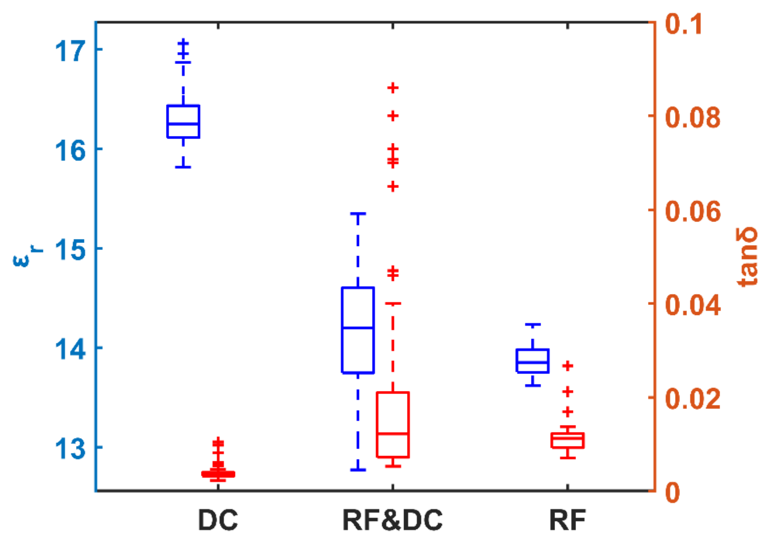

Figure 6: The relative permittivity (ε_r) and dielectric loss tangent (tan δ) of AlScN deposited by three modes of sputtering, measured under 1 V_{AC} and 1 kHz

Figure 6 shows the impact of the sputtering mode on the dielectric response of AlScN thin films. As the sputtering mode changes from fully DC to fully RF sputtering, the permittivity decreases, and the dielectric loss increases. The RF&DC co-sputtered films show the greatest variation in both permittivity and tanδ among the three film types, which is attributed to increased non-uniformity across the film from the mixed deposition and the increased chamber pressure. Both the permittivity and the tanδ for all film types has increased with respect to pure AlN which prior literature puts at 9.2 and 0.002 respectively.[28] The DC sputtered AlScN shows a 77% increase in permittivity compared to AlN, while RF&DC and RF sputtered films show a 54% and 51% permittivity increase respectively. The increases in permittivity of AlScN over AlN is attributed to the increased degree of bond ionicity and enhanced polarizability in valence electrons with the addition of scandium into AlN.[29] The permittivity for all film types lies within the range that has previously been reported for AlScN with a Sc concentration between 20 to 30 at% measured at 1 kHz – between 14 to 21.[17,29,30] Therefore, this suggests that the target concentration of 25 at% is maintained in the sputtered films. The dielectric loss for the DC sputtered films is the lowest, with an average of 0.0046, while the RF&DC films had the highest loss with an average of 0.021. The average loss for the DC films is consistent with the response seen in other AlScN films,[31] while the range for the other two film types extends beyond the expected values for these compounds, which again points to the impact of non-uniformity in the co-sputtered films.

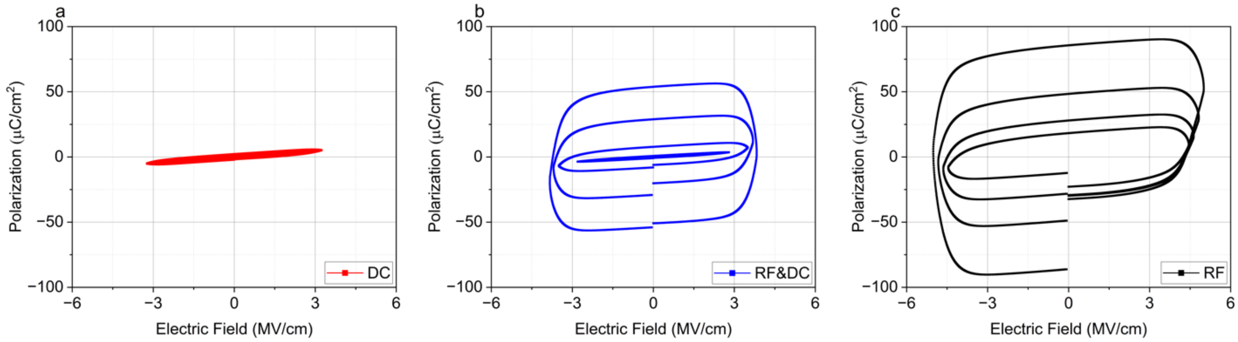

Figure 7: PE hysteresis loops taken at 100 Hz over a range of different excitation voltages for **(a.)** DC sputtered films, **(b.)** RF&DC co-sputtered films, and **(c.)** RF sputtered films

The polarization-electric field (PE) hysteresis loops of the AlScN films processed by different methods show distinctively unique features. **Figure** 7**a** shows a typical PE loop for the films grown by DC sputtering, where a linear response is maintained with minimal change in slope or loop opening, until around 3 MV/cm before breakdown. The maximum polarization reached was also the lowest among the three film types, on the order of a few μC/cm^2. The low leakage in the PE loop for the DC films is consistent with the lower loss seen in the dielectric measurements in **Figure** 6. The lack of a discrete local maxima in the concurrent current response also demonstrates that these DC films show limited indications of ferroelectric switching prior to breakdown.

In the RF&DC co-sputtered films, there was a drastic transition from linear dielectric behavior to open, square loops that exhibit a clear and sudden change in slope. **Figure** 7**b** shows a representative PE loop for these films. There is a clear transition from minor to major loops, with clear coercive fields and remnant polarizations visible in the major loop. The maximum remnant polarization and coercive field reached prior to breakdown were on average 35 μC/cm^2 and 3.7 MV/cm, respectively. Current measurements taken concomitantly to the PE measurements**,** exhibit a slight increase in current at the coercive field consistent with ferroelectric behavior. However, the loop tips are blunted with no clear sign of saturation polarization observed prior to electric breakdown. Limited saturation polarization is commonly observed in AlScN films, where the coercive field is often close to the breakdown strength of the material.[16] Additionally, the remnant polarization for these films is significantly lower than what has previously been reported for AlScN, suggesting that some portions of the films do not exhibit a ferroelectric response, which fits with what is observed for the DC films. Overall, the PE results suggest that ferroelectric switching occurs in the co-sputtered films, which will be described further in the following sections on PUND and Rayleigh analysis.

The RF sputtered films have on average the largest polarization value among the three sample types, with clear signs of switching. PE loops for a quintessential RF film are shown in **Figure** 7**c**. Again, a clear change in slope can be seen just prior to hitting the coercive field which would not occur in a linear dielectric. The maximum remnant polarization and coercive field reached prior to breakdown for one specific sample were approximately 90 $\mu C/cm^2$ and 5.1 MV/cm, and the averages of these two values across all electrodes were 53 $\mu C/cm^2$ and 4.8 MV/cm, respectively. Another indication of ferroelectric switching can be seen in current-field loops of the films, where there is a clear maximum in the current at the coercive field. Additionally, the electric field that the material could withstand prior to breakdown and the polarization the material could reach also increase with drive voltage in the RF sputtered films. However, the leakage currents for these films tended to be larger than the co-sputtered or DC films, which can hinder polarization switching.

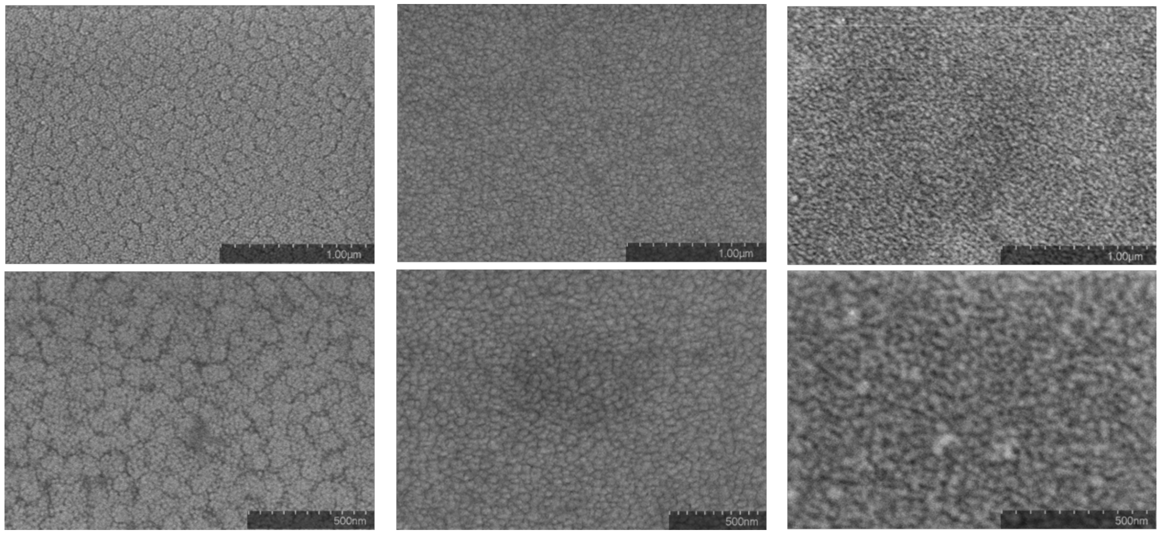

Figure 8. SEM planar morphology images using the same length scale, (a) DC sputtered, **(b)** RF&DC sputtered, and **(c)** RF sputtered. The three different films have varied surface morphology. The DC sputtered films have the largest average grain size of approximately 89 nm, while the RF&DC co-sputtered film has an average grain size of ~42.58 nm. Co-deposited films have a surface morphology that is similar to the RF sputtered films. The average grain size for RF sputtered films is approximately ~49.13 nm

The increase in leakage current could be attributed to the reduced average grain size and grooved grain boundaries seen in the RF films. Of all of the film types the DC films have the largest average grain size, shown in the planar SEM images in **Figure 8.** Differences in the strain state of the films from the deposition impingement or differences in the interface with the bottom electrode that occurred during RF sputtering could also play a role both in the switching and leakage current behaviors.[32] Overall, with increasing RF sputtering and decreasing DC sputtering contributions, the AlScN thin films show increased indications of ferroelectric switching and increased leakage.

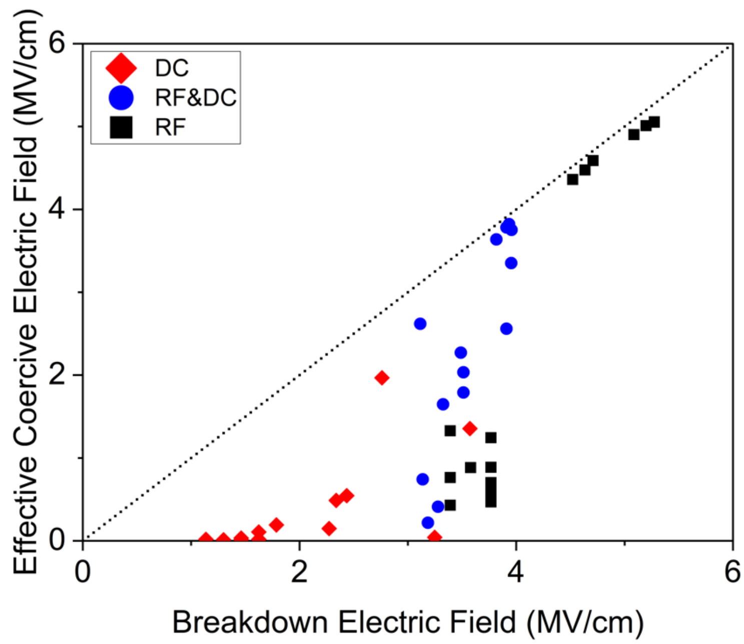

Figure 9. Summary of effective coercive fields ($E_{C,f}$) and breakdown fields (E_{BD}) for films deposited by DC, RF&DC, and RF sputtering. Each data point represented one device. The dotted line, representing 1:1 ratio between E_C and E_{BD}, is added for reference

Comparing the coercive field and the breakdown strength of films deposited through different sputtering methods provides further perspective on the stark differences between the electric response of each film type. **Figure 9** shows the effective coercive field ($E_{C,f}$) versus the breakdown electric field (E_{BD}), defined as the minimum electric field that caused breakdown for a device made from each film type. The effective coercive field is obtained from the positive electric field intercept (where the polarization equals zero) for the PE loop corresponding to the maximum excitation voltage before breakdown. This is only an effective value as the DC films never gave indications of ferroelectric switching or reaching the coercive voltage prior to breakdown, but interceptive value is still extracted from the PE loops for comparison.

The breakdown strength of films with different deposition conditions are clustered in distinct regions. The DC sputtered films show the lowest $E_{C,f}$ and E_{BD} with more than half of the electrodes having an $E_{C,f}$ close to 0, corresponding to the linear dielectric behavior observed in the ferroelectric and dielectric measurements. The RF&DC films have a narrower distribution of E_{BD}, with a sharp increase in $E_{C,f}$ with the highest values of $E_{C,f}$ approaching E_{BD}. These results indicate that a mixture of sputtering methods could be used to separate the coercive and breakdown fields. For the RF sputtered film, there is a bimodal distribution in breakdown strength and coercive field. The group with the lower E_{BD} has $E_{C,f}$ that is significantly lower than E_{BD}. In the second grouping of RF films not only is the breakdown strength higher, but the $E_{C,f}$ is almost identical to the E_{BD}. The multimodality of RF films suggests that there is non-uniformity in the film consistent with the increase in the range of the dielectric loss and the increased leakage current. For the second grouping, there is a 4.7 V (0.177 MV/cm) difference between the coercive field and breakdown. The highest breakdown strength observed in this study occurs for the RF films at 5.27 MV/cm. With an increasing portion of RF sputtering, the E_{BD} has an increasing trend, but the E_C values also approach the breakdown fields.

Positive-Up-Negative-Down (PUND) measurements provide further insight into the polarization response in AlScN films deposited by different sputtering modes. PUND provides a means to differentiate between polarization and other contributions to current, which are often comingled or convoluted in PE measurements. As this method is generally applied, it is assumed that the first negative pulse switches the polarization entirely, then any subsequent pulse must contain only spurious contributions to current.[33] By calculating the difference in polarizations between the first and the second pulse, P_{PUND}, can be used to approximate the remnant polarization (P_R). However, in this work, given the close proximity between the coercive field and breakdown in the AlScN films as discussed previously, the PUND measurements are not taken at a single value above the coercive field but rather taken from 0 to the breakdown field to ensure that the polarization response is captured. Thus, it cannot be assumed the response is ferroelectric or that the films have reached the coercive field until the polarization saturates. Additionally, as measurements are taken with progressively increasing fields up to breakdown this could include the onset of degradation.

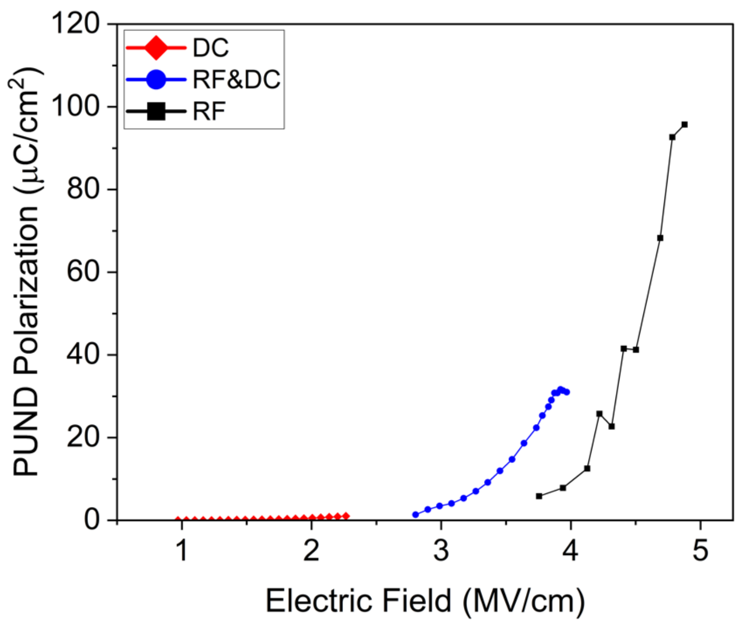

Figure 10: PUND Polarization (P_{PUND}) extracted from PUND measurement for each of the three sputtered film types up to the breakdown strength

Figure 10 shows the combined PUND polarizations for each film, obtained through a series of measurements with progressively increasing excitation voltages. Examples of the raw PUND data are given for each sample type in **Figure 11**, note that the P_{PUND} is the difference between P^ and P*.

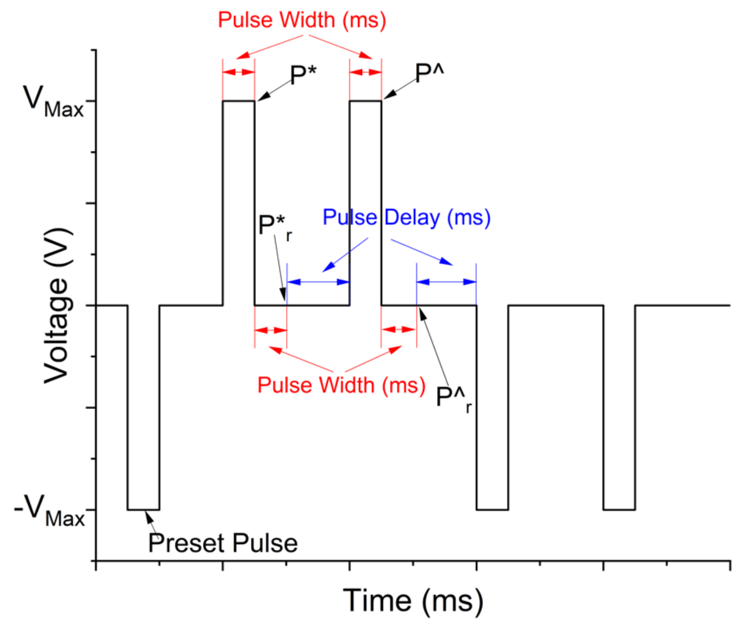

Figure 11. The pulse profile used in PUND measurements, adapted from Vision software

All the films show an increase in P_{PUND} from 0 to their respective maximum values over a narrow range of electric fields. The rapid increase in the polarization response in the RF films is consistent with the sudden transition from minor loops to major loops shown in the PE hysteresis loops in **Figure 7**. In the DC sputtered film, the maximum P_{PUND} was approximately 1 μC/cm^2, similar to the linear dielectric behavior observed in the PE loops. Again, the limited maximum polarization compared to what would be expected for $Al_xSc_{1-x}N$ (~120 μC/cm^2)[34] and the lack of clear saturation further supports that these films do not exhibit ferroelectric switching. The maximum P_{PUND} for the RF&DC co-sputtered film was 35 μC/cm^2 at an excitation field of 4 MV/cm, again on par with the major PE loops. Unlike the DC films, the co-sputtered films exhibit a saturation of the PUND polarization beyond 3.8 MV/cm. In this electric field region, increasing the voltage no longer produces differences in the polarization measurement, indicating that the coercive field has likely been reached. On average this saturation region extends to approximately 0.2 MV/cm prior to breakdown and no degradation is observed in the polarization prior to breakdown. This narrow region of stable saturated P_{PUND} agrees with the close proximity of E_C and E_{BD} seen in **Figure 9**. The maximum P_{PUND} was 98 μC/cm^2 at 4.6 MV/cm for the RF sputtered films. Similar to the co-sputtered films, there is a region of saturation in the polarization prior to breakdown. Overall, the P_R values and their trends at different excitation voltages were consistent with the hysteresis loops. Thus, the PUND results provide further evidence for ferroelectricity in RF and co-sputtered films.

Rayleigh analysis provides further support for the polarization measurements and aids in assessing the ferroelectric domain switching response. In ferroelectric materials, a Rayleigh response is attributed to the movement of domain walls, domain clusters, or phase boundaries.[35–37] The reversible and irreversible Rayleigh coefficients are determined from the slope and intercept of the permittivity under different AC fields. The reversible Rayleigh coefficient provides information about the reversible contributions to the dielectric response that comes from a combination of the intrinsic lattice response and domain wall movements with minimal dielectric loss.[37,38] The irreversible Rayleigh coefficient accounts for energy loss and hysteresis in the dielectric response due to irreversible domain wall movements under small signal AC fields.[37,38] Rayleigh analysis is taken using fields that are significantly below the coercive field, in sub-switching regime, which is beneficial for materials that exhibit large leakage currents or have a propensity to break down near the coercive field, as is the case for AlScN.[37]

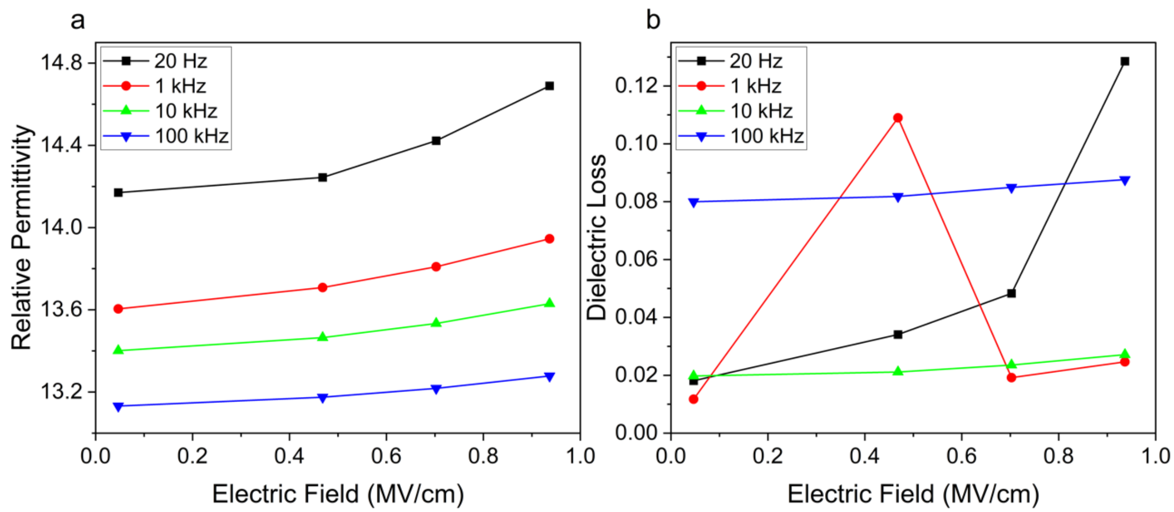

Figure 12. (a.) Permittivity and **(b.)** dielectric loss tangent as a function of frequency from 20 Hz to 100 kHz under small signal AC electric field for RF&DC co-sputtered AlScN sample

Figure 12. shows the change in permittivity and tanδ, respectively, with varying applied AC electric fields for the RF&DC co-sputtered films. Above 20 Hz, the permittivity increases approximately linearly with increasing electric field, indicative of ferroelectric domain or phase boundary contributions to the permittivity. There is also an inverse correlation between frequency and permittivity, which could be indicative of domain wall pinning.[39] The dielectric loss tangent has a limited slope, with the exception of measurements at 20 Hz. Similar trends are also seen for the RF sputtered films. There is a linearly increasing relationship for both permittivity and dielectric loss with applied AC voltage and the same inverse response between frequency and permittivity. Overall, the Rayleigh response in films with RF sputtering is consistent with the ferroelectric responses found through PE and PUND measurements.

While the trends for RF and RF&DC sputtered films are similar, the DC films exhibit a different response. shows the permittivity and loss tangent, respectively, as a function of applied AC electric fields for the DC sputtered sample. The AC field dependence of the permittivity is still linear, but the slope is greatly reduced compared to the other two film types, and the dielectric loss tangent is also comparatively smaller. These results are consistent with the linear dielectric behavior seen in the PE hysteresis measurements and the unsaturated PUND polarization measurements, showing that there is limited switchability in the DC films.

Figure 13 below shows the reversible and irreversible Rayleigh coefficients calculated from the slope and intercept of the permittivity under different AC fields**.** There is a higher irreversible Rayleigh coefficient in the RF films than in the DC films, which indicates more hysteretic and non-linear behaviors, consistent with the ferroelectric response seen in the PE and PUND measurements of the RF sputtered film. As for the reversible Rayleigh response, DC film had the largest coefficient consistent with having the largest relative permittivity, as shown in **Figure 6**. For the frequency dependence of Rayleigh coefficients, there is also a reduction in Rayleigh response, both reversible and irreversible, which could indicate less domain wall contributions at higher frequencies.[40–42] These results are consistent with the previously-reported frequency-dependent dielectric responses of $Al_{0.84}Sc_{0.16}N$, where the permittivity decreases with increasing measurement frequency.[43] From Rayleigh behavior, it can be inferred that there are different contributions to permittivity between DC and RF sputtered films indicative of differing ferroelectric contributions.

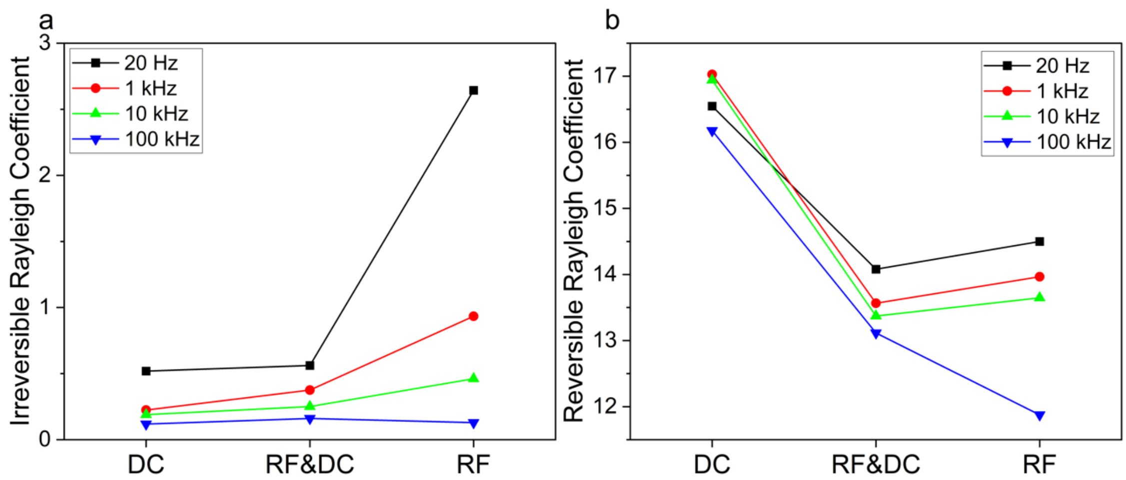

Figure 13 (a) Irreversible and **(b)** reversible Raleigh coefficients for sputtered films under different AC field frequencies

The difference in sputtering type (RF, DC, vs RF&DC co-sputtering) leads to the variations in the ferroelectric responses among the sputtered $Al_{0.75}Sc_{0.25}N$ thin films. Here we see that using DC sputtering from a ceramic target produces only linear dielectric responses, while prior work has shown that DC reactive sputtering from Al and Sc metal targets in nitrogen still displays ferroelectricity.[44] One potential reason for the difference in propensity for ferroelectricity may stem from the difference in energy of the sputtered particulates impacting the film morphology and substrate interface. This is supported by the clear difference in the grain size and surface morphology shown by SEM in **Error! Reference source not found.8**. Furthermore, the absence in ferroelectricity in the DC sputtered films in this work, and the presence of ferroelectricity in RF films, suggests that the coercive field for the DC materials lies beyond the breakdown field. Thus, by increasing the contributions from RF sputtering the coercive field could be reduced consistent with previous reports of using a 50-50 mixture of RF and DC power supply to the Al metal target to reduce the coercive field.[23] Moving forward it is critical to determine how the trends in coercive field and breakdown with sputtering method observed in this work change as the percentage of scandium is increased or the film thickness is decreased.

3.6 Conclusions

In summary, this paper compares the differences in the ferroelectric and dielectric response of AlScN thin films deposited using three different growth modes (RF, DC, RF&DC co-sputtered). Clear indications of ferroelectricity were observed in RF sputtered films with E_C and P_R values of 98 μC/cm^2 and 4.6 MV/cm, respectively. The DC sputtered films displayed linear dielectric behavior and minimal observable ferroelectricity response. The results from PUND measurements and Rayleigh analysis support the presence of ferroelectricity in RF sputtered films and the absence of it in DC sputtered films. RF&DC co-sputtered films also display ferroelectricity, with an approximately 1 MV/cm lower average E_C and half of P_R compared to RF sputtered films. The decrease in ferroelectric response is balanced by the benefits of increased separation between the coercive field and the breakdown strength in the co-sputtered films. Therefore, sputter depositing using multiple modes concurrently is promoted as a route to increase the separation of the coercive and breakdown fields in AlScN thin films.

3.7 References

1. Sun, T. *et al.* Determination of the Impact of Sputtering Mode on the Ferroelectric Response of AlScN Thin Films. *APL Materials*.
2. Mikolajick, T. *et al.* Next generation ferroelectric materials for semiconductor process integration and their applications. *Journal of Applied Physics* **129**, 100901 (2021).

3. Gharavi, P., Olsson, R. H. & Stach, E. Interfacial Origins of Electrical Breakdown Strength Enhancement in AlScN through Multilayer Structure. *Microscopy and Microanalysis* **30**, ozae044.531 (2024).
4. Zhang, Y., Zhu, Q., Tian, B. & Duan, C. New-Generation Ferroelectric AlScN Materials. *Nanomicro Lett* **16**, 227 (2024).
5. Satoh, S., Ohtaka, K., Shimatsu, T. & Tanaka, S. Crystal structure deformation and phase transition of AlScN thin films in whole Sc concentration range. *Journal of Applied Physics* **132**, 025103 (2022).
6. Sandu, C. S. *et al.* Abnormal Grain Growth in AlScN Thin Films Induced by Complexion Formation at Crystallite Interfaces. *physica status solidi (a)* **216**, 1800569 (2019).
7. Yang, F. Physics of Ferroelectric Wurtzite $Al_{1-x}Sc_xN$ Thin Films. *Adv Elect Materials* **11**, 2400279 (2025).
8. Zhang, Y., Zhu, Q., Tian, B. & Duan, C. New-Generation Ferroelectric AlScN Materials. *Nano-Micro Lett.* **16**, 227 (2024).
9. Fichtner, S., Wolff, N., Lofink, F., Kienle, L. & Wagner, B. AlScN: A III-V semiconductor based ferroelectric. *Journal of Applied Physics* **125**, 114103 (2019).
10. Wolff, N. *et al.* Demonstration and STEM Analysis of Ferroelectric Switching in MOCVD-Grown Single Crystalline $Al_{0.85}Sc_{0.15}N$. *Advanced Physics Research* **3**, (2024).
11. Yasuoka, S. *et al.* Effects of deposition conditions on the ferroelectric properties of $(Al_{1-x}Sc_x)N$ thin films. *Journal of Applied Physics* **128**, 114103 (2020).

12. Yasuoka, S. *et al.* Probing of Polarization Reversal in Ferroelectric (Al,Sc)N Films Using Single- and Tri-Layered Structures With Different Sc/(Al+Sc) Ratio. *Adv Materials Inter* 2400627 (2024) doi:10.1002/admi.202400627.
13. Gu, X. *et al.* Analysis of Heterostructure Formation of Abnormally Oriented Grains in Sputter-Deposited AlScN Films and Its Impact on Bulk Acoustic Wave Devices. *ACS Appl. Mater. Interfaces* **16**, 53106–53115 (2024).
14. Wang, W. B. *et al.* AlScN thin film based surface acoustic wave devices with enhanced microfluidic performance. *J. Micromech. Microeng.* **26**, 075006 (2016).
15. Huang, X. *et al.* Interface structures of $Al_{0.85}Sc_{0.15}N$-on-Si thin films grown by reactive magnetron sputtering upon post-growth cyclic rapid thermal annealing. *Journal of Applied Physics* **135**, 095304 (2024).
16. Kurinec, S. K., Schroeder, U., Subramanyam, G. & Olsson Iii, R. H. Emerging ferroelectric thin films: Applications and processing. in *Handbook of Thin Film Deposition* 405–454 (Elsevier, 2025). doi:10.1016/B978-0-443-13523-1.00003-X.
17. Yazawa, K. *et al.* Anomalously abrupt switching of wurtzite-structured ferroelectrics: simultaneous non-linear nucleation and growth model. *Mater. Horiz.* **10**, 2936–2944 (2023).
18. Wang, D. *et al.* Ferroelectric Switching in Sub-20 nm Aluminum Scandium Nitride Thin Films. *IEEE Electron Device Lett.* **41**, 1774–1777 (2020).
19. Tokita, Y., Tsutsui, K., Kakushima, K., Wakabayashi, H. & Hoshii, T. A Ferroelectric Property Tailoring Method of $Al_{0.7}Sc_{0.3}N$ Films by Sputter-Deposition Pressure. *ECS Meeting Abstracts* **MA2023-01**, 1786 (2023).

20. Guido, R. *et al.* Thermal Stability of the Ferroelectric Properties in 100 nm-Thick $Al_{0.72}Sc_{0.28}N$. *ACS Appl. Mater. Interfaces* **15**, 7030–7043 (2023).
21. Ryoo, S. K. *et al.* Investigation of Optimum Deposition Conditions of Radio Frequency Reactive Magnetron Sputtering of $Al_{0.7}Sc_{0.3}N$ Film with Thickness down to 20 nm. *Adv Elect Materials* **8**, 2200726 (2022).
22. Kim, K. D. *et al.* Evolution of the Ferroelectric Properties of AlScN Film by Electrical Cycling with an Inhomogeneous Field Distribution. *Adv Elect Materials* **9**, 2201142 (2023).
23. Pirro, M. *et al.* Ferroelectric Considerations on Co-Sputtered 30% AlScN with Different DC+RF Ratios. in *2021 Joint Conference of the European Frequency and Time Forum and IEEE International Frequency Control Symposium (EFTF/IFCS)* 1–3 (IEEE, Gainesville, FL, USA, 2021). doi:10.1109/EFTF/IFCS52194.2021.9604316.
24. Zhang, J. *et al.* Leakage Study of Ferroelectric AlScN Capacitors Prepared on Different Bottom Electrodes. in *2024 9th International Conference on Integrated Circuits and Microsystems (ICICM)* 82–86 (IEEE, Wuhan, China, 2024). doi:10.1109/ICICM63644.2024.10814445.
25. Drury, D., Yazawa, K., Zakutayev, A., Hanrahan, B. & Brennecka, G. High-Temperature Ferroelectric Behavior of $Al_{0.7}Sc_{0.3}N$. *Micromachines* **13**, 887 (2022).
26. Yassine, M. *et al.* Influence of structural properties on the ferroelectric behavior of hexagonal AlScN. *Journal of Applied Physics* **132**, 114101 (2022).
27. Khánh, N. Q. *et al.* Effect of process parameters on co-sputtered $Al_{(1-x)}Sc_xN$ layer's properties: Morphology, crystal structure, strain, band gap, and piezoelectricity. *Materials Science in Semiconductor Processing* **169**, 107902 (2024).

28. Thorp, J. S., Evans, D., Al-Naief, M. & Akhtaruzzaman, M. The dielectric properties of aluminium nitride substrates for microelectronics packaging. *J Mater Sci* **25**, 4965–4971 (1990).

29. Casamento, J. *et al.* AlScN High Electron Mobility Transistors: Integrating High Piezoelectric, High K Dielectric, and Ferroelectric Functionality. in *2023 IEEE BiCMOS and Compound Semiconductor Integrated Circuits and Technology Symposium (BCICTS)* 132–136 (IEEE, Monterey, CA, USA, 2023). doi:10.1109/BCICTS54660.2023.10310921.

30. Wingqvist, G. *et al.* Increased electromechanical coupling in w−$Sc_xAl_{1-x}N$. *Applied Physics Letters* **97**, 112902 (2010).

31. Zukauskaite, A. *et al.* Microstructure and dielectric properties of piezoelectric magnetron sputtered w-$Sc_xAl_{1-x}N$ thin films. *Journal of Applied Physics* **111**, 093527 (2012).

32. McMitchell, S. R. C. *et al.* Engineering Strain and Texture in Ferroelectric Scandium-Doped Aluminium Nitride. *ACS Appl. Electron. Mater.* **5**, 858–864 (2023).

33. Alikin, D. *et al.* Defining ferroelectric characteristics with reversible piezoresponse: PUND switching spectroscopy PFM characterization. *Nanotechnology* **35**, 175702 (2024).

34. Kim, K.-H., Karpov, I., Olsson, R. H. & Jariwala, D. Wurtzite and fluorite ferroelectric materials for electronic memory. *Nat. Nanotechnol.* **18**, 422–441 (2023).

35. Becker, M. T., Burkhardt, C. J., Kleiner, R. & Koelle, D. Impedance spectroscopy of ferroelectrics: The domain wall pinning element. *Journal of Applied Physics* **132**, 044104 (2022).

36. Bintachitt, P. *et al.* Collective dynamics underpins Rayleigh behavior in disordered polycrystalline ferroelectrics. *Proc. Natl. Acad. Sci. U.S.A.* **107**, 7219–7224 (2010).

37. Eitel, R. E. Rayleigh Law Response in Ferroelectric Ceramics: Quantifying Domain Wall Dynamics and Structural Relationships. in *2007 Sixteenth IEEE International Symposium on the Applications of Ferroelectrics* 319–323 (IEEE, Nara-city, Japan, 2007). doi:10.1109/ISAF.2007.4393253.

38. Lou, X. J. *et al.* Effect of polarization fatigue on the Rayleigh coefficients of ferroelectric lead zirconate titanate thin films: Experimental evidence and implications. *Applied Physics Letters* **105**, 102907 (2014).

39. Taylor, D. V. & Damjanovic, D. Evidence of domain wall contribution to the dielectric permittivity in PZT thin films at sub-switching fields. *Journal of Applied Physics* **82**, 1973–1975 (1997).

40. Damjanovic, D. Stress and frequency dependence of the direct piezoelectric effect in ferroelectric ceramics. *Journal of Applied Physics* **82**, 1788–1797 (1997).

41. Liu, L., Rojac, T., Damjanovic, D., Di Michiel, M. & Daniels, J. Frequency-dependent decoupling of domain-wall motion and lattice strain in bismuth ferrite. *Nat Commun* **9**, 4928 (2018).

42. Marquardt, R. *et al.* Domain Wall Movement in Undoped Ferroelectric HfO_2: A Rayleigh Analysis. *ACS Appl. Electron. Mater.* **5**, 3251–3260 (2023).

43. Zhu, W. *et al.* Strongly temperature dependent ferroelectric switching in AlN, $Al_{1-x}Sc_xN$, and $Al_{1-x}B_xN$ thin films. *Applied Physics Letters* **119**, 062901 (2021).

44. Wall, J. M. & Yan, F. Sputtering Process of $Sc_xAl_{1-x}N$ Thin Films for Ferroelectric Applications. *Coatings* **13**, 54 (2022).

CONCLUSIONS & FUTURE WORK

The work demonstrates the synthesis of AlScN solid solution thin films and hafnium bottom electrodes, with further characterization done to demonstrate the structural, chemical, and electrical response of the associated thin films.

Chapter 1 demonstrates the synthesis of AlScN solid solutions on (100) Si substrates without the use of a seed layer, establishing a pathway for integration with standard semiconductor platforms. X-ray diffraction revealed that films with scandium content below 21 at.% exhibit strong c-axis orientation, as evidenced by clear (0002) and (0004) peaks. These films also showed smooth surfaces without faceting, which is critical for piezoelectric applications that rely on uniform strain distribution and minimal acoustic losses. As the Sc target power was increased from 100 W to 150 W, the Sc concentration rose from 21 to 27 at.%, and the oxygen content increased from 15 to 21 at.%. These compositional changes coincided with a reduction in the intensity of the (0002) and (0004) reflections and the emergence of surface facets, indicating a degradation in crystallinity. This suggests that although higher Sc content is desirable to enhance piezoelectric coefficients, it also introduces a trade-off by promoting structural disorder and oxygen incorporation, which can degrade piezoelectric performance and long-term reliability.

Ferroelectric and dielectric measurements conducted in on AlScN solid solutions synthesized on hafnium bottom electrodes in Chapter 2 illustrated that the electrical behavior of AlScN films is strongly dependent on the sputtering mode. Films deposited using RF sputtering exhibited a remanent polarization (Pr) of 98 $\mu C/cm^2$ and a coercive field (Ec) of 4.6 MV/cm, indicating clear ferroelectric switching. These characteristics are beneficial for non-volatile ferroelectric memory applications that require high polarization for charge storage. In contrast, films deposited using DC sputtering showed minimal polarization switching and primarily linear dielectric behavior, making them unsuitable for ferroelectric applications but potentially stable for capacitive or insulating layers. Co-sputtered RF&DC films presented intermediate behavior, with a Pr approximately half that of RF-only films and a coercive field reduced by ~1 MV/cm. While this reduction in polarization may limit their use in high-density memory, the larger separation between the coercive field and breakdown strength makes these films promising for applications requiring high endurance and low operating voltages, such as ferroelectric field-effect transistors (FeFETs) or tunable dielectrics.

To further advance the control over AlScN film quality and minimize the impact of process-induced defects, future work will focus on the use of pulsed laser deposition (PLD) as an alternative growth method. PLD processes allow the thin film to maintain the target stoichiometry and isolate the influence of RF chamber bias. This approach will allow for a more controlled study of defect formation, particularly electrical leakage-inducing defects, and B-site (nitrogen / oxynitride) stoichiometry. Investigations will be of low-dimensional (<20 nm) AlScN films to be relevant to future piezoelectric and ferroelectric device applications where space is limited. A key target is to achieve films with a low dielectric loss ($\tan \delta < 0.02$) while maintaining measurable ferroelectric switching. Special attention will be given to the role of reactive nitrogen species (N^+, N_2) and their interaction with the AlScN lattice under RF-biased conditions. Structural, chemical, and electrical characterization will be used to evaluate the effects of RF bias on Sc incorporation, oxidation behavior, film texture, and leakage current. This line of investigation aims to expand the processing window for high-performance AlScN films by enabling scalable growth of thin, low-defect, ferroelectric layers that maintain desirable crystallographic and electrical properties. Success in this area could establish PLD as a complementary technique for AlScN integration in low-voltage ferroelectric memory, neuromorphic computing elements, and miniaturized piezoelectric sensors.

AUTHOR DECLARATIONS & ACKNOWLEDGEMENTS

ACKNOWLEDGEMENTS:

This work was supported as part of the Center for 3D Ferroelectric Microelectronics Manufacturing, an Energy Frontier Research Center funded by the U.S. Department of Energy, Office of Science, Basic Energy Sciences under Award # DE-SC0021118.

This work was performed in part at the Georgia Tech Institute for Electronics and Nanotechnology (IEN) under the SEED Grant support. The IEN is a member of the National Nanotechnology Coordinated Infrastructure (NNCI), which is supported by the National Science Foundation (Grant ECCS-1542174). John Wellington-Johnson was funded by a National Science Foundation Graduate Research Fellowship Program under grant number (NSF grant DGE-2039655).

John Wellington-Johnson would like to acknowledge the financial support from the National GEM Consortium and LAM Research Corporation. We would also like to gratefully acknowledge the guidance and training from Margo Staruch of the U.S. Naval Research Laboratory for the sputter processing.